1 **Title: H3.1K27M-induced misregulation of the TSK/TONSL-H3.1 pathway causes**

2 **genomic instability**

3

4 **Authors:**

5 Wenxin Yuan[1, †], Yi-Chun Huang[1, †], Chantal LeBlanc[1], Axel Poulet[1,2,3], Devisree Valsakumar[4,5],

6 Josien C. van Wolfswinkel[1,2,3], Philipp Voigt[5] and Yannick Jacob[1,6,*]

7

8 [†] These authors contributed equally to this manuscript.

9 * Corresponding author e-mail: yannick.jacob@yale.edu

10

11 **Affiliations:**

12 [1] Yale University, Department of Molecular, Cellular and Developmental Biology, Faculty of Arts

13 and Sciences; 260 Whitney Avenue, New Haven, Connecticut 06511, USA.

14 [2] Yale Stem Cell Center, Yale School of Medicine, New Haven, CT 06511, USA.

15 [3] Center for RNA science and medicine, Yale School of Medicine, New Haven. CT 06511, USA.

16 [4] Wellcome Centre for Cell Biology, School of Biological Sciences, University of Edinburgh,

17 Edinburgh EH9 3BF, United Kingdom.

18 [5] Epigenetics Programme, Babraham Institute, Cambridge CB22 3AT, United Kingdom.

19 [6] Yale Cancer Center, Yale School of Medicine; New Haven, Connecticut 06511, USA

20

21

22

23

Abstract

The oncomutation lysine 27-to-methionine in histone H3 (H3K27M) is frequently identified in tumors of patients with diffuse midline glioma-H3K27 altered (DMG-H3K27a). H3K27M inhibits the deposition of the histone mark H3K27me3, which affects the maintenance of transcriptional programs and cell identity. Cells expressing H3K27M are also characterized by defects in genome integrity, but the mechanisms linking expression of the oncohistone to DNA damage remain mostly unknown. In this study, we demonstrate that expression of H3.1K27M in the model plant *Arabidopsis thaliana* interferes with post-replicative chromatin maturation mediated by the H3.1K27 methyltransferases ATXR5 and ATXR6. As a result, H3.1 variants on nascent chromatin remain unmethylated at K27 (H3.1K27me0), leading to ectopic activity of TONSOKU (TSK), which induces DNA damage and genomic alterations. Elimination of TSK activity suppresses the genome stability defects associated with H3.1K27M expression, while inactivation of specific DNA repair pathways prevents survival of H3.1K27M-expressing plants. Overall, our results suggest that H3.1K27M disrupts the chromatin-based mechanisms regulating TSK/TONSL activity, which causes genomic instability and may contribute to the etiology of DMG-H3K27a.

Introduction

DMG-H3K27a, a type of brain cancer that mostly affects children, is characterized by a very poor prognosis with fewer than 10% of patients surviving more than two years after diagnosis (*1*). Approximately 80% of DMG patients are carriers of a somatic K27M mutation in one of the histone H3 genes (*2, 3*). The H3K27M mutation can occur in genes encoding different histone H3 variants: replication-dependent H3.1 or H3.2 (H3.1/H3.2 variants hereafter referred to as H3.1), and replication-independent H3.3 (*3, 4*). Initial work has shown that expression of H3.1K27M or H3.3K27M leads to a decrease of histone H3 lysine 27 tri-methylation (H3K27me3) by inhibiting the activity of the H3K27 methyltransferase POLYCOMB REPRESSIVE COMPLEX 2 (PRC2) (*5-8*). In cancer cells, H3.1K27M and H3.3K27M are both expressed amid a much larger contingent of wild-type H3.1 and H3.3 proteins, but the mutated histones inhibit PRC2 in a dominant-negative manner (*5, 7*), which accounts for the drastic loss of H3K27me3 observed in DMG-H3K27a cells.

A large majority of the work on oncogenic H3K27M mutations has centered on the consequences of decreased H3K27me3 levels and the subsequent effects on transcriptional regulation. However, the disruption of other cellular activities by H3K27M may have been overlooked, as PRC2 activity in mammals and *Drosophila melanogaster* is responsible for all levels of methylation at H3K27 (*9-11*). Mono- and di-methylation at H3K27 (H3K27me1/2), which are together much more abundant than H3K27me3 in mouse embryonic stem cells (*10*), have cellular functions that are independent of H3K27me3 (*10, 12, 13*). In line with this, it has been confirmed that levels of H3K27me1/2 at specific loci are also reduced by the H3K27M oncomutation in H3K27M-expressing cell lines (*14*). Consequently, there is a major increase in unmethylated histone H3 at K27 (H3K27me0), to the point

68   where it can become the most dominant form of H3K27 (*15*). Importantly, PRC2 inhibition by

69   H3K27M leads to a large increase of K27me0 on both H3.1 and H3.3 variants (*15*).

70

71   Lysine 27 of newly synthesized H3.1 proteins is unmethylated prior to incorporation of H3.1 into

72   chromatin during DNA replication (*16, 17*). Recently, it was shown in the model plant *Arabidopsis*

73   *thaliana* (Arabidopsis) that H3.1K27me0 is specifically required for the recruitment of the conserved

74   DNA repair protein TONSOKU (TSK; known as TONSL in animals) to replication forks (*18*). In

75   mammals, TONSL has been shown to initiates homologous recombination-mediated resolution of

76   stalled or broken replication forks (*19-22*). DNA repair via TSK/TONSL needs to be tightly regulated

77   in dividing cells of plants and animals by histone methyltransferases, which methylate post-replicative

78   chromatin to prevent TSK/TONSL activity outside of stalled or broken replication forks (*18, 23*). In

79   the absence of the post-replicative chromatin maturation step that inhibits TSK/TONSL, genome

80   instability is observed in a TSK/TONSL-dependent manner (*18*). Chromatin-based regulation of TSK

81   in plants has been shown to depend on the redundant activity of the H3.1K27 mono-methyltransferases

82   ATXR5 and ATXR6 (ATXR5/6) (*24, 25*), which mono-methylate H3.1K27 to prevent binding of TSK

83   to H3.1 through its conserved tetratricopeptide repeat (TPR) domain (*18, 25*). In Arabidopsis, where

84   unregulated TSK activity has been extensively studied, this results in many phenotypes, including

85   widespread genomic amplification of heterochromatic sequences (hereafter referred to as

86   heterochromatin amplification), DNA damage, and loss of transcriptional silencing (*18, 25-27*).

87

88   Genomic instability is a defining characteristic of many cancer cells (*28*), including H3.1K27M and

89   H3.3K27M tumors (*29-33*). The frequent co-occurrence of specific secondary mutations associated

90   with H3.1K27M and H3.3K27M (*32*), and the defects in genome integrity in cancer cells harboring

4

91 these mutations, suggest a model where expression of H3K27M generates a DNA error-prone

92 environment that can induce and/or accelerate tumorigenesis (*33*). Accordingly, specific DNA repair

93 pathways and DNA repair pathway choice have been shown to be affected by H3K27M (*30, 33*), but

94 a direct link between the oncohistone and misregulation of DNA repair proteins has not yet been

95 established. In this work, we demonstrate that expression of H3.1K27M disrupts the regulation of the

96 TSK/TONSL-H3.1 DNA repair pathway. Using Arabidopsis as a model system for K-to-M mutations

97 on H3 (*34*), we show that expression of H3.1K27M induces DNA damage. This effect of H3.1K27M

98 is due to its ability to block the activity of ATXR5/6, which results in an increase of H3.1K27me0 in

99 chromatin. Similarly to *atxr5/6* mutants, increased levels of H3.1K27me0 induce heterochromatin

100 amplification and loss of transposon silencing. By inactivating TSK in H3.1K27M-expressing plants,

101 we were able to confirm that ectopic activity of the TSK-H3.1 DNA repair pathway is responsible for

102 disrupting genome integrity. In addition, loss of the DNA repair proteins MRE11 and RAD51 in

103 H3.1K27M-expressing plants results in synthetic lethality, thus suggesting specific vulnerabilities in

104 cells expressing H3.1K27M. We discuss the implications of these results obtained in the Arabidopsis

105 model and how they could translate to a better understanding of the etiology of cancers characterized
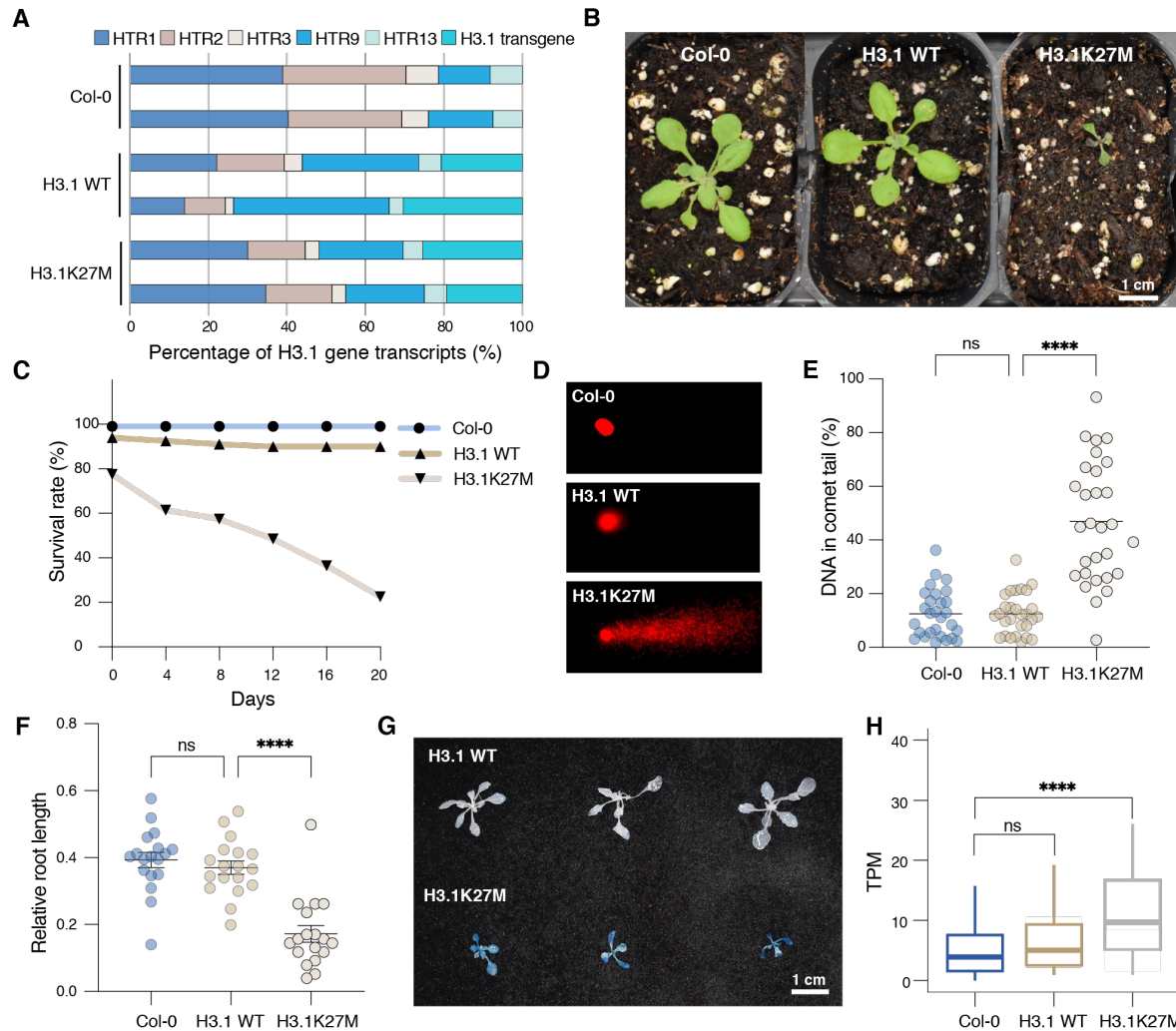
106 by H3.1K27M expression.

107

108

109 **Results**

110 **H3.1K27M expression induces genomic instability in Arabidopsis**

111 To explore the biological mechanisms affected by an H3K27M mutation, we created transgenic

112 Arabidopsis plants expressing H3.1K27M under a native H3.1 promoter (H3.1$_{prom}$::H3.1K27M) in the

113 wild-type Columbia-0 (Col-0) background, which also expresses a normal set of endogenous histone

114   H3.1 from five H3.1 genes (*35*). As a control, we also created transgenic plants expressing wild-type

115   H3.1 (H3.1$_{prom}$::H3.1 WT). RNA-seq analysis showed that H3.1K27M transcripts corresponded to

116   ~20% of all H3.1 transcripts (Fig. 1A), indicating that a majority of H3.1 proteins in the transgenic

117   plants are wild type. This approach provides the opportunity to evaluate the phenotypic and molecular

118   effects caused by H3.1K27M expression in a model system where H3-variant-specific effects on

119   genome stability and DNA repair have been previously characterized (*18*).

120

121   The H3.1K27M transgenic plants demonstrated significant developmental defects compared to Col-0

122   and wild-type H3.1 controls (H3.1 WT), exhibiting stunted growth and much smaller and narrower

123   leaves compared to the control plants (Fig. 1B and fig. S1A). The germination and survival rates of

124   H3.1K27M plants were severely affected, with most plants dying before day 20 (Fig. 1C). In addition,

125   the H3.1K27M plants displayed an increase in anthocyanin content, which is commonly associated

126   with cellular stress (fig. S1B) (*36*). To assess for the presence of DNA damage, we conducted comet

127   assays and found a significant increase in tail DNA percentage for H3.1K27M-expressing plants

128   compared to Col-0 and H3.1 WT controls, which is indicative of DNA breaks (Fig. 1, D and E). We

129   also found that H3.1K27M plants were hypersensitive to the genotoxic effects of methyl

130   methanesulfonate (MMS) (Fig. 1F and fig. S1C). We then used the disrupted beta-glucuronidase

131   (*uidA*/*GUS*) system to directly assess the frequency of homologous recombination events in our

132   transgenic plants (*37*). In this system, homology-directed repair is required to reconstitute a gene that

133   can produce a functional GUS protein. Our results showed that GUS activity was much stronger in

134   H3.1K27M transgenic plants, indicating higher levels of homology-directed repair at the *GUS* gene

135   (Fig. 1G). In accord with these results, RNA-seq experiments in Col, H3.1 WT and H3.1K27M plants

136   showed that many DNA damage response genes are upregulated when H3.1K27M is expressed (Fig.

Figure 1. H3.1K27M expression induces developmental defects and DNA damage in Arabidopsis. A Relative abundance of H3.1 gene transcripts. **B** Morphological phenotypes of Col-0, H3.1 WT and H3.1K27M plants. **C** Survival rates of Col-0, H3.1 WT and H3.1K27M plants. **D** Representative comet assay images. **E** Quantification of DNA percentage in the comet tails. Horizontal bars indicate the mean. Welch's ANOVA followed by the Dunnett's T3 test: **** $p < 0.0001$, ns = not significantly different. **F** Relative root length of seedlings grown on ½ MS plates with 100 µg/ml MMS compared to the average root length of seedlings grown on plates without MMS. Each dot represents one individual T1 plant. Horizontal bars indicate the mean. SEM is shown. One-way ANOVA with Tukey's multiple comparison test: **** $p < 0.0001$, ns = not significantly different. **G** Representative image of histochemical staining of reporter plants for GUS activity. Blue areas indicate that a functional reporter gene has been restored via a somatic recombination event. **H** RNA-seq data showing relative transcript levels of 158 DNA damage response genes (Table S1) measured by transcripts per million (TPM). Wilcoxon test with Bonferroni correction: **** $p < 0.0001$, ns = not significantly different.

7

155   1H and Table S1). Taken together, these results indicate that expression of H3.1K27M in Arabidopsis

156   generates DNA damage.

157

158   **H3.1K27M expression inhibits the histone methyltransferase activity of PRC2 and ATXR5/6**

159   In human cells, H3K27M mutations interfere with PRC2 in a dominant-negative manner, which

160   prevents the spreading of H3K27me3 (*5, 7*). Given the high degree of conservation between plant and

161   animal histone H3 variants and PRC2 complexes (*35, 38*), we hypothesized that expression of

162   H3K27M in plants would also block PRC2 activity. To verify this, we performed immunostaining and

163   observed a drastic decrease of H3K27me3 in nuclei from H3.1K27M-expressing plants compared to

164   Col-0 and H3.1 WT (Fig. 2A). We also assessed H3K27me3 levels by chromatin immunoprecipitation

165   sequencing combined with exogenous chromatin spike-in (ChIP-Rx) to normalize the H3K27me3

166   signal between samples. Profiles for H3K27me3 over protein-coding genes showed a large decrease

167   in H3K27me3 in H3.1K27M plants compared to Col-0 and H3.1 WT in both high- and low-expressing

168   genes (Fig. 2B and fig. S2A). Together, these results suggest that expression of the oncohistone

169   H3.1K27M disrupts PRC2 activity in plants similarly to human cells.

170

171   In plants, H3K27 methylation is also catalyzed by the SET domain-proteins ATXR5/6, which

172   specifically mono-methylate the H3.1 variant (*24, 25*). K-to-M mutations on histone H3 has been

173   shown to inhibit the activity of multiple histone methyltransferases (*39*), so we predicted that

174   expression of H3.1K27M in Arabidopsis may not only inhibit PRC2, but also ATXR5/6. To validate

175   this hypothesis, we first performed ChIP-Rx analysis and observed a large decrease in H3K27me1

176   signal over heterochromatin in H3.1K27M-expressing plants compared to Col-0 and H3.1 WT plants

177   (Fig. 2C and fig. S2B). Immunofluorescence staining using an H3K27M antibody showed that the

8
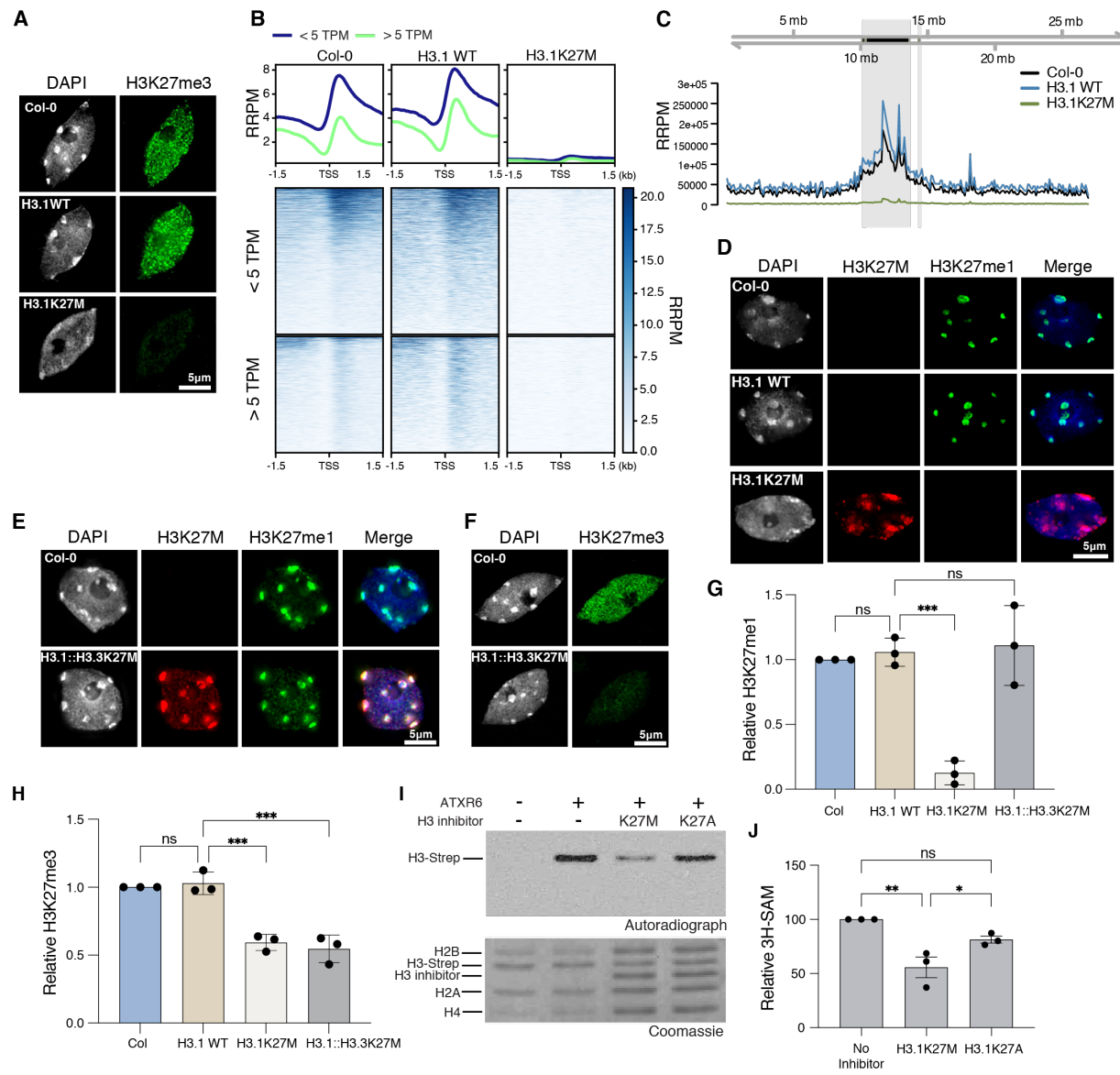
Figure 2. H3.1K27M-expressing plants exhibit loss of ATXR5/6-mediated H3K27me1. **A** Staining of leaf nuclei with an anti-H3K27me3 antibody and DAPI. **B** ChIP-seq profiles and heatmaps of normalized H3K27me3 signal over protein-coding genes grouped by level of expression (< 5 and > 5 TPM) in reference-adjusted reads per million (RRPM). TSS, transcription start site. **C** ChIP-Rx normalized H3K27me1 signal using 100 kb windows over chr 5. The pericentromeric region is shown in gray. **D** to **F** Staining of leaf nuclei with anti-H3K27M and anti-H3K27me1 (D and E) or anti-H3K27me3 antibodies (F) and DAPI. **G** and **H** Relative Western blot quantification of H3K27me1 (G) and H3K27me3 (H) levels in leaf total histones. One-way ANOVA with Tukey's multiple comparison test: *** $p < 0.001$, ns = not significantly different. **I** Representative *in vitro* histone methyltranferase assay using ATXR6 and recombinant nucleosomes containing plant H3.1-strep. Nucleosomes containing H3K27M or H3K27A (H3 inhibitor) were added to the reactions. **J** Quantification of the relative amount of ^{3}H-SAM incorporated into the H3.1-strep substrate. Each dot represents one independent experiment. Bars represent the mean. SEM is shown. One-way ANOVA with Tukey's multiple comparison test: ** $p = 0.0040$, * $p = 0.0459$, ns = not significantly different.

9

193 mutated histone is enriched at chromocenters (Fig. 2D), as expected, because H3.1 proteins are

194 concentrated within heterochromatic domains in somatic cells of Arabidopsis (*40, 41*). Staining with

195 an H3K27me1 antibody showed the characteristic enrichment of this histone mark at chromocenters

196 in Col-0 and H3.1 WT plants (*42*), but a drastic reduction in H3.1K27M-expressing plants (Fig. 2D).

197 To demonstrate that the loss of H3K27me1 was due to ATXR5/6 inhibition, we generated transgenic

198 plants expressing H3.1$_{prom}$::H3.3K27M in the wild-type Col-0 background. As ATXR5/6 are unable

199 to interact with H3.3 (*24*), we hypothesized that they would not be inhibited by H3.3K27M, but that

200 PRC2 complexes would be negatively impacted as they can interact with both H3.1 and H3.3 in plants.

201 As expected, we found that the level of H3K27me1 in H3.1$_{prom}$::H3.3K27M plants was similar to Col-

202 0, indicating that the presence of H3.3K27M did not inhibit ATXR5/6 (Fig. 2E). We did, however,

203 find that the level of H3K27me3 was reduced in these plants (Fig. 2F), thus confirming that PRC2

204 activity in Arabidopsis is disrupted by H3.3K27M. Consistent with the immunostaining experiments,

205 we observed a large decrease of H3K27me1 in H3.1K27M-expressing plants, but not in

206 H3.1$_{prom}$::H3.3K27M plants, in total histone samples extracted from leaves (Fig. 2G and fig. S2C). In

207 contrast, a reduction in H3K27me3 was seen in both H3.1K27M and H3.1$_{prom}$::H3.3K27M plants (Fig.

208 2H and fig. S2C).

209

210 Previous studies have shown that H3K27M acts in a dominant-negative manner by directly inhibiting

211 the catalytic subunit (i.e., EZH2) of PRC2 (*5, 7, 43, 44*). Based on this, we hypothesized that the effect

212 of H3.1K27M on H3K27me1 levels may work through a similar direct inhibitory mechanism on

213 ATXR5/6. To test this, we performed *in vitro* histone methyltransferase (HMT) assays with and

214 without H3.1K27M nucleosomes serving as potential ATXR6 inhibitors. Our results showed

215 decreased levels of methylated H3.1 substrates when H3.1K27M nucleosomes were present in the

216   reaction (Fig. 2, I and J). In contrast, H3.1K27A (lysine 27-to-alanine) had a smaller inhibitory effect

217   than H3.1K27M on ATXR6 (Fig. 2, I and J), which is comparable to the effects of these two H3.1

218   mutants on mammalian PRC2 activity *in vitro* (*45*). Overall, our data indicate that, in the presence of

219   H3.1K27M, ATXR5/6-mediated mono-methylation of H3.1K27 is inhibited, leading to widespread

220   loss of H3.1K27me1 in the Arabidopsis genome.

221

222   **H3.1K27M induces genomic instability defects similarly to *atxr5/6* mutants**

223   Loss of H3.1K27me1 in *atxr5/6* mutants leads to various heterochromatic phenotypes, including

224   chromocenter decondensation, heterochromatin amplification (i.e., an increase in the copy number of

225   transposons and other repetitive elements) and loss of transposon silencing (*25-27*). As H3.1K27M-

226   expressing plants show a massive reduction of H3K27me1 (Fig. 2, C and D), we hypothesized that

227   they would have heterochromatic defects similar to *atxr5/6* mutants. DAPI staining of nuclei from

228   H3.1K27M-expressing plants revealed a hollowed sphere conformation of chromocenters

229   characteristic of nuclei from *atxr5/6* mutant plants (Fig. 3, A and B) (*46*). Flow cytometry analyses

230   showed that H3.1K27M plants exhibit broader peaks corresponding to endoreduplicated nuclei, a

231   phenotype associated with heterochromatin amplification and also observed in *atxr5/6* mutants (Fig.

232   3, C and D) (*26*). In accord with this, whole-genome sequencing of H3.1K27M-expressing plants

233   revealed that heterochromatic regions are amplified similarly to *atxr5/6* mutants (Fig. 3E). Finally,

234   RNA-seq analysis indicated transcriptional reactivation of transposable elements (TEs) normally

235   silenced in a Col-0 background, like in *atxr5/6* mutants (Fig. 3F).

236

237   In all our assays (Fig. 3, A to F), we observed an increase in the magnitude of heterochromatic defects

238   in H3.1K27M plants compared to *atxr5/6* mutants. This observation is in line with the morphological

11
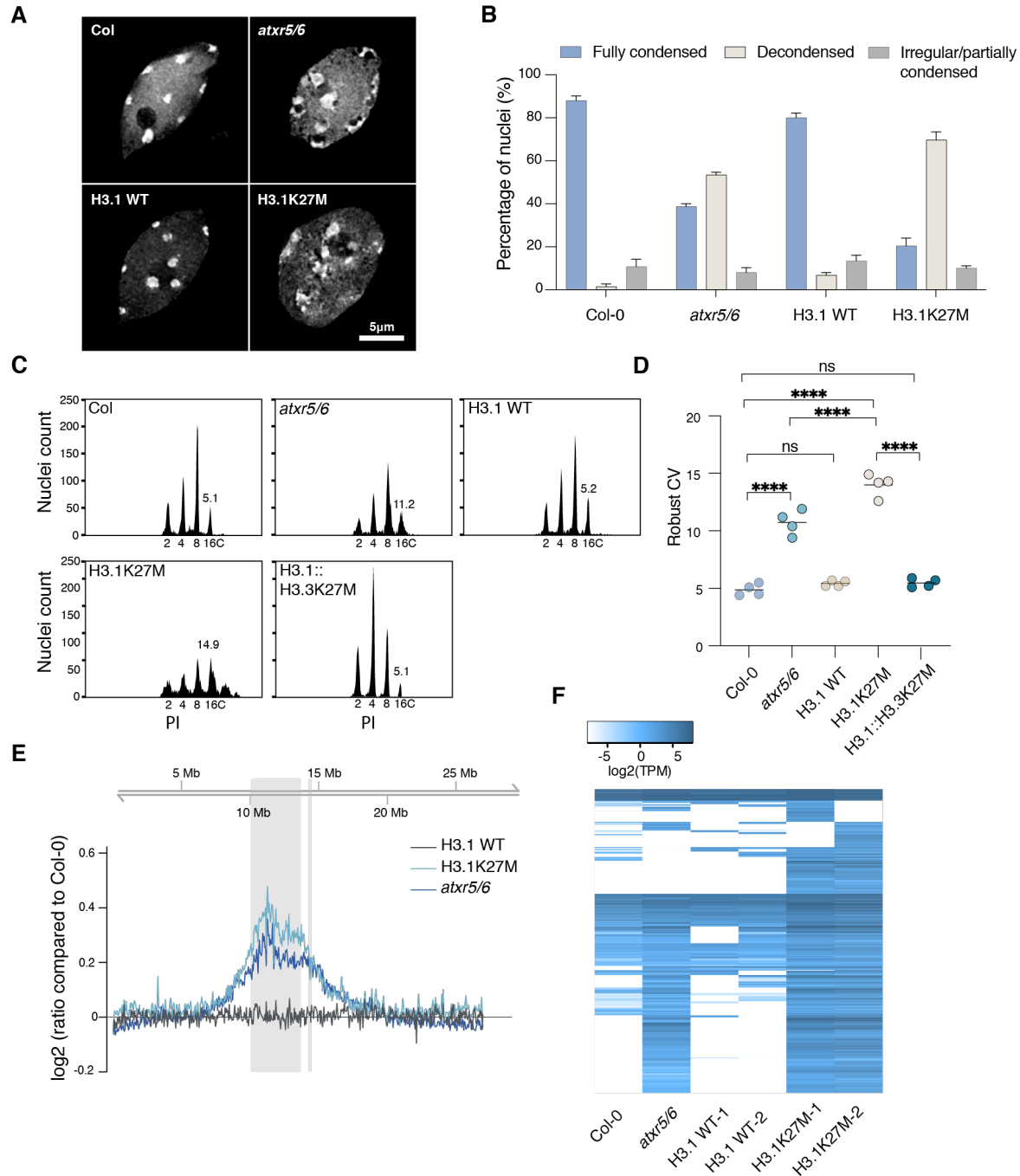
Figure 3. H3.1K27M induces heterochromatin defects similarly to *atxr5/6* mutants. A Leaf interphase nuclei stained with DAPI. **B** Quantification of chromocenter appearance of nuclei from experiment in panel A. **C** Flow cytometry profiles of leaf nuclei stained with propidium iodide (PI). Ploidy levels of the nuclei are shown below the peaks. The numbers above the 16C peaks indicate the robust coefficient of variation (CV). **D** Robust CV quantification of 16C peaks. Each dot represents an individual plant. The mean is shown. One-way ANOVA with Tukey's multiple comparison test: **** $p < 0.0001$, ns = not significantly different. **E** Chromosomal view (Chr 5) of DNA-seq reads. The pericentromeric region is highlighted in gray. **F** Heat map showing the relative expression levels of TEs induced in H3.1K27M plants (Table S2).

12

248   comparison of these two genetic backgrounds, with *atxr5/6* mutants showing only a mild leaf

249   developmental phenotype while H3.1K27M-expressing plants are drastically smaller and struggle to

250   make it to the adult stage (fig. S3A). The well-characterized *atxr5/6* double mutant used in our

251   experiments is a hypomorphic mutant, as *ATXR6* expression from the mutant allele is only reduced

252   compared to wild-type plants (*25*). We use this particular mutant for our studies because complete

253   elimination of ATXR5 and ATXR6 activity is lethal in Arabidopsis (*47*). The phenotypic variation

254   between H3.1K27M-expressing plants and *atxr5/6* mutants may be linked to the difference in

255   H3.1K27me1 levels between the two genetic backgrounds. This hypothesis is supported by Western

256   blot analyses showing that H3.1K27me1 levels are much lower in H3.1K27M-expressing plants than

257   *atxr5/6* mutants in two-week old plants (fig. S3B and C). In summary, our results indicate that

258   expression of H3.1K27M mimics the phenotypes of *atxr5/6* mutants, and that *in vivo* levels of

259   H3.1K27me1 may dictate the severity of these phenotypes.

260

261   **H3.1K27M induces genomic instability in a TSK-dependent manner**

262   In plants, ATXR5/6 methylate newly synthesized H3.1 variants inserted on chromatin to induce post-

263   replicative chromatin maturation, a key regulatory step that prevents the activity of the DNA repair

264   protein TSK by inhibiting its binding to chromatin (*18, 24, 25, 48*). TSK is recruited to nascent

265   chromatin via its conserved TPR domain, which specifically interacts with H3.1 proteins unmethylated

266   at K27 (H3.1K27me0) (*18*). In the absence of post-replicative chromatin maturation via H3.1K27me1,

267   TSK is thought to either remain associated with chromatin post-replication or interact with it *de novo*.

268   Genomic instability in *atxr5/6* mutants has been shown to be dependent on TSK activity (*18*), thus

269   suggesting that the phenotypes observed in H3.1K27M-expressing plants may similarly rely on this

270   protein.

271 To investigate a potential link between TSK and the H3.1K27M-associated phenotypes, we introduced

272 the H3.1K27M transgene into a *tsk* mutant background (T-DNA insertional mutant SALK_034207).

273 We found that elimination of TSK activity suppressed most of the growth abnormalities and early

274 lethality associated with H3.1K27M expression in the Col-0 background (Fig. 4, A and B). Though

275 the *tsk*/H3.1K27M plants remained smaller than Col-0, H3.1 WT, *tsk* and *tsk*/H3.1 WT plants, they

276 were able to progress to the reproductive phase of growth, which was never observed when H3.1K27M

277 was expressed in the Col-0 background. Flow cytometry analyses of *tsk*/H3.1K27M plants showed

278 suppression of heterochromatin amplification as represented by the loss of broad peaks and confirmed

279 by whole-genome sequencing (Fig. 4C and fig. S4, A and B). Chromocenter decondensation was also

280 found to be suppressed in H3.1K27M-expressing plants lacking TSK (Fig. 4D). A possible mechanism

281 of suppression is that H3K27me1 levels are restored to wild-type levels in a *tsk* mutant, however, this

282 was ruled out by immunostaining and Western blot analyses (Fig. 4, D and E and fig. S4C). We also

283 tested if suppression of the phenotypes associated with loss of H3.1K27me1 was due to lower

284 H3.1K27M transgene expression in *tsk* mutants. We performed RT-qPCR and found no significant

285 difference between Col-0 and *tsk* (fig. S4D). It is interesting to note that complete suppression of the

286 genomic instability phenotypes in *tsk*/H3.1K27M plants does not lead to plants morphologically

287 resembling Col-0 (Fig. 4, A and B). This is likely due to the loss of H3K27me3 in these plants caused

288 by inhibition of PRC2 (Fig. 4F). Similar phenotypes were observed in the H3.1$_{prom}$::H3.3K27M plants,

289 where H3K27me3 is reduced, but not H3K27me1 (Fig. 2, E to H and fig. S4E).

290

291 Our findings suggest that H3.1K27M inhibits ATXR5/6 in a dominant-negative manner, which leads

292 to an increase in K27me0 on wild-type H3.1 proteins. This results in chromatin binding of TSK outside

293 of its normal spatial and temporal boundaries, and as a consequence, DNA damage. However, it is

14
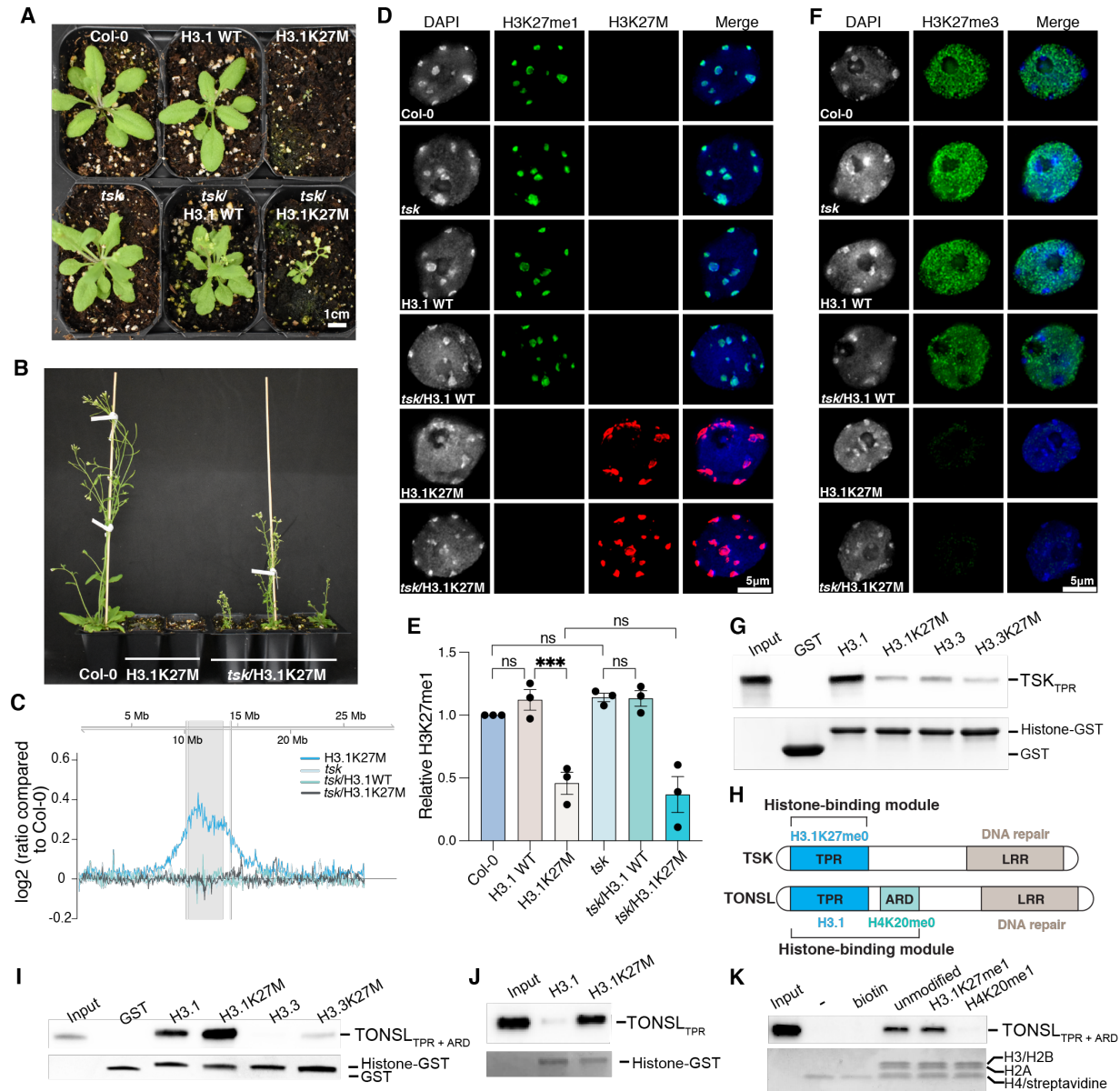
Figure 4. H3.1K27M causes genomic instability by inducing ectopic TSK activity. A and **B** Morphological phenotypes of Col-0, *tsk*, H3.1 WT, H3.1K27M, *tsk*/H3.1 WT and *tsk*/H3.1K27M plants. **C** Chromosomal view (Chr 5) of DNA-seq reads. The pericentromeric region is highlighted in gray. **D** Immunostaining of leaf nuclei with anti-H3K27M and anti-H3K27me1 antibodies. DNA is stained with DAPI. **E** Western blot quantification showing relative H3K27me1 levels in total histones extracted from leaves. One-way ANOVA with Tukey's multiple comparison test: *** $p < 0.001$, ns = not significantly different. **F** Staining of leaf nuclei with an anti-H3K27me3 antibody and DAPI. **G** Peptide pull-down assay using the TPR domain of TSK (TSK$_{TPR}$) and GST-tagged histone peptides (aa 1 to 58). **H** Domain architecture of plant and animal TSK/TONSL. TPR: Tetratricopeptide Repeats, ARD: Ankyrin Repeat Domain, LRR: Leucine-Rich Repeats. **I** and **J** Pull-down assay with TPR + ARD domains (TONSL$_{TPR + ARD}$) (I) or the TONSL TPR domain only (TONSL$_{TPR}$) (J) with GST-tagged histone peptides (aa 1 to 58). **K** Pull-down assay of TONSL$_{TPR + ARD}$ with biotinylated recombinant nucleosomes.

15

307   also possible that H3.1K27M increases the interaction of TSK with H3.1, thus leading to DNA damage

308   at genomic regions where H3.1K27M is inserted. Analysis of the structure of the TSK_{TPR}-H3.1

309   complex does not support this mechanism, as H3.1K27 is positioned within a polar pocket that makes

310   it unfavorable for binding hydrophobic entities such as the sidechain of methionine (*18*). We verified

311   this by performing *in vitro* binding assays and confirmed that the interaction of TSK with H3.1 is

312   reduced when lysine 27 is replaced with methionine (Fig. 4G). We also conducted split-luciferase

313   complementation assays and detected luminescence signals when TSK_{TPR}-cLuc was coexpressed with

314   H3.1 WT-nLuc, but not with H3.1K27M-nLuc (fig. S4, F and G). Altogether, these findings support

315   a model where, in plants, genomic instability is not due to a direct interaction between H3.1K27M

316   nucleosomes and TSK, but instead arises from increased levels of H3.1K27me0 leading to ectopic

317   TSK activity.

318

319   To assess if the inhibitory effect of H3.1K27M and H3.1K27 methylation on TSK binding is conserved

320   in the mammalian TONSL ortholog, we performed binding assays using the complete histone

321   interaction module of TONSL (TPR and ARD domains) or the TPR domain only (Fig. 4H).

322   Interestingly, we found that mouse $TONSL_{TPR+ARD}$ and $TONSL_{TPR}$ displayed increased binding to

323   H3.1K27M compared to wild-type H3.1 (Fig. 4I-J), and that the interaction of $TONSL_{TPR+ARD}$ with

324   histones is restricted by H4K20me1, but not H3.1K27me1 (Fig. 4K). These results suggest that

325   H3.1K27M insertion on chromatin leads to ectopic TSK/TONSL activity in both plants and animals,

326   but via a different mechanism.

327

328

329

H3.1K27M-expressing plants are hypersensitive to the loss of specific DNA repair proteins

H3.1K27M expression has similar effects on genomic stability as *atxr5/6* mutants. Our previous work showed that various phenotypes in *atxr5/6* mutants are either enhanced or suppressed by the loss of specific DNA repair pathways (*18*). For example, loss of RAD51 (involved in homologous recombination) or Pol θ (key player in theta-mediated end joining [TMEJ]) in *atxr5/6* mutants enhances the growth defects of these plants. This is likely due to an increased reliance on repair of damaged DNA resulting from higher levels of H3.1K27me0 and unregulated TSK activity. In Col-0, mutations in *RAD51* or *POLQ* (coding for POL θ) have no effects on plant growth (*18*). These observations suggest that plants expressing H3.1K27M may also be hypersensitive to the loss of DNA repair pathways due to high levels of DNA damage caused by the oncohistone. To test this, H3.1K27M was first introduced into heterozygous *rad51* mutants (T0 plants), as homozygous *rad51* mutants are sterile and therefore cannot be transformed by Agrobacterium using the flower dip method (*49*). Transformation of heterozygous *rad51* mutants with constructs expressing H3.1K27M or H3.1 WT resulted in 1% (1/95) and 25% homozygous *rad51* mutants (T1 plants), respectively (Fig. 5A). The near absence of homozygous *rad51* mutants in the T1 generation of H3.1K27M plants strongly suggests that homologous recombination is a major contributor to DNA repair and plant/cell viability in H3.1K27M-expressing plants. We could not replicate this strategy to assess the contribution of TMEJ via Pol θ in H3.1K27M plants, as *polq* mutants cannot be transformed via Agrobacterium-mediated flower dipping (*50*). As TMEJ relies on resected DNA as a substrate to initiate DNA repair (*51, 52*), we tested the effect of MRE11 in plants expressing H3.1K27M. MRE11 is a key component of the MRE11–RAD50–NBS1 (MRN) complex responsible for DNA end resection (*53*). Similarly to the experiment using *rad51*, we introduced H3.1K27M and H3.1 WT into heterozygous T0 plants since homozygous *mre11* mutants are sterile (*54*). We only recovered 2% (1/59) homozygous *mre11*

17
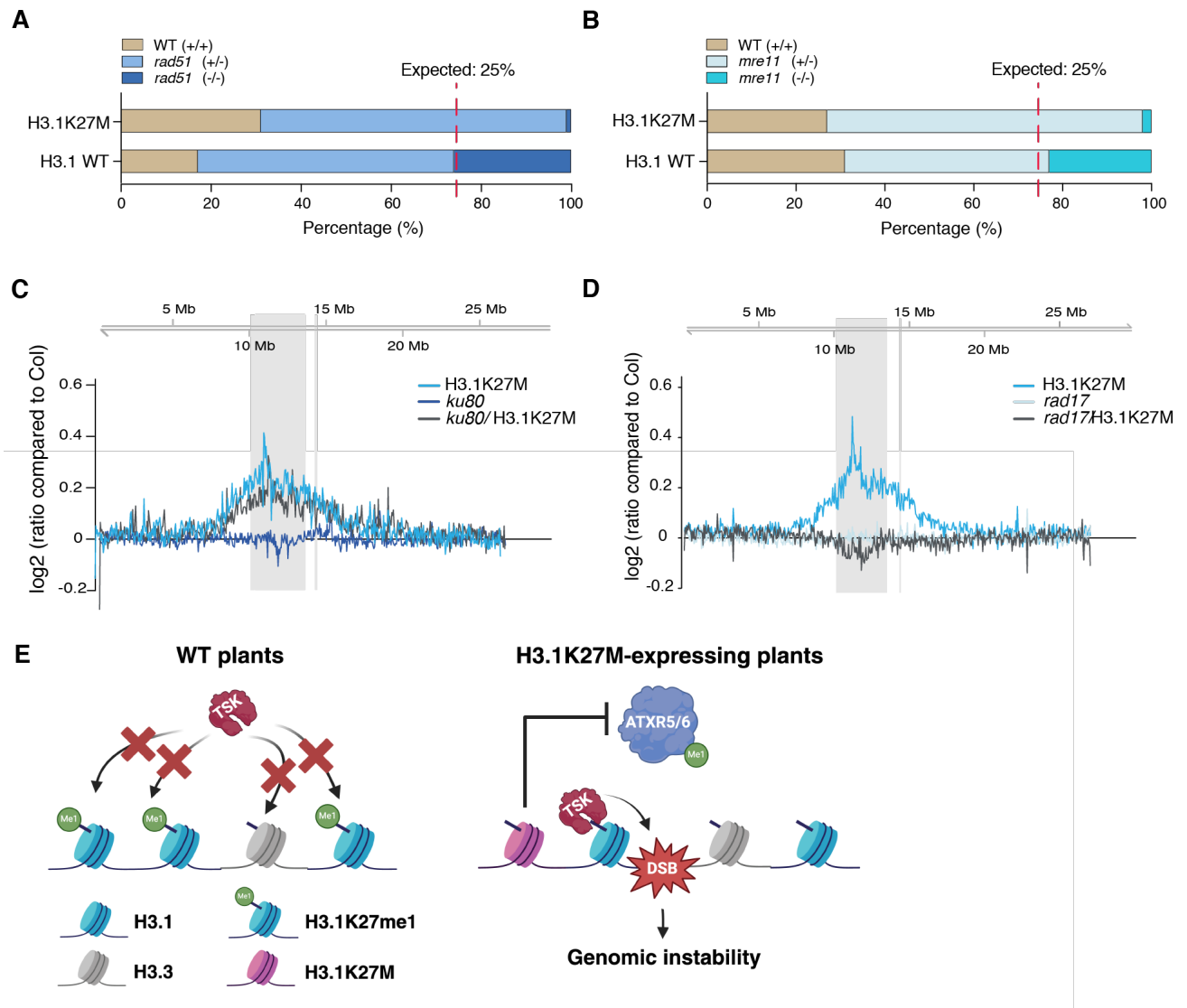
Figure 5. Differential effects of H3.1K27M expression in DNA repair mutants. A and **B** Genotypes of T1 transgenic plants resulting from transformation of H3.1 WT and H3.1K27M into *rad51* heterozygous (*rad51* [+/-]) (A) and *mre11* heterozygous (*mre11* [+/-]) (B) T0 plants. **C** and **D** Chromosomal view (Chr 5) of DNA-seq reads. The pericentromeric region is highlighted in gray. **E** Model depicting how H3.1K27M expression leads to genomic instability by increasing the levels of H3.1K27me0, which causes misregulation of TSK.

365 mutants among the T1 progeny (Fig. 5B). In contrast, transformation of H3.1 WT resulted in 23% of

366 the T1 transformants being homozygous *mre11* mutant, which is close to the expected 25% for a

367 transgene with no effect on plant survival. This result suggests that DNA resection mediated by the

368 MRN complex specifically contributes to the survival of H3.1K27M plants. To further explore if

369 H3.1K27M-expressing plants respond like *atxr5/6* mutants to the absence of key DNA repair

370 pathways, we tested non-homologous end joining (NHEJ) by directly transforming H3.1K27M or

371 H3.1 WT into homozygous *ku80* mutants. The absence of Ku80 in plants expressing H3.1K27M did

372 not enhance growth defects or suppress heterochromatin amplification, which parallels the phenotypes

373 observed in *atxr5/6 ku80* triple mutants (Fig. 5C and fig. S5, A and B) (*18*). Finally, we assessed the

374 impact of RAD17 in H3.1K27M-expressing plants. As observed in *atxr5/6 rad17* triple mutants (*18*),

375 loss of RAD17 in H3.1K27M plants abolished heterochromatin amplification while having no

376 measurable effects on plant growth (Fig. 5D and fig. S5, B and C). Overall, these results demonstrate

377 that the phenotypes of H3.1K27M-expressing plants and *atxr5/6* mutants are modulated by the same

378 DNA repair proteins, and that expression of the oncohistone in Arabidopsis generates a dependence

379 on specific DNA repair pathways for survival.

380

381

382 **Discussion**

383 Genomic instability is associated with DMG-H3K27a and the H3K27M oncomutation (*29-33*).

384 However, underlying mechanisms directly linking H3K27M to DNA damage in these cancers remains

385 mostly unexplored. In this study, we showed using Arabidopsis as a model that expression of

386 H3.1K27M replicates the genomic instability phenotypes observed in *atxr5/6* mutants, which are

387 caused by misregulation of the TSK-H3.1 DNA repair pathway (*18*). Loss of H3.1K27me1 in *atxr5/6*

388   mutants or H3.1K27M-expressing plants prevents post-replicative chromatin maturation, leaving H3.1

389   variants unmethylated. As H3.1K27me0 serves to recruit TSK to chromatin, a model emerges where

390   ectopic binding of TSK to chromatin in H3.1K27M-expressing cells, or its retention on chromatin

391   post-replication, induces DNA damage leading to genomic instability (Fig. 5E). More work will be

392   needed to understand the mechanism by which TSK induces DNA damage when it is present on

393   chromatin outside of its normal path of entry and exit during chromatin replication.

394

395   An important question is whether the findings of this study in plants translate to human cells, and if

396   they can help us understand the etiology of DMG-H3K27a. In mammals, post-replicative chromatin

397   maturation restricting TONSL activity has been shown to depend on SET8-catalyzed H4K20me1,

398   which blocks the interaction between TONSL and chromatin (*23*). H4K20me0 is read by the TONSL

399   ARD domain, which is not present in plant TSK orthologs (SET8 orthologs are also absent in plants)

400   (*55*). Both TSK and TONSL contain the TPR domain that mediates the specific interaction with the

401   H3.1 variant (*18*). TSK binding to H3.1 is inhibited by methylation of K27 in plants (*18*), but our *in*

402   *vitro* results suggest that the TPR domain of TONSL is insensitive to mono-methylation at H3.1K27.

403   This indicates that in contrast to plants, misregulation of TONSL activity in mammals may not occur

404   as a result of genome-wide loss of H3K27 methylation due to PRC2 inhibition by H3.1K27M.

405   However, and again in contrast to plant TSK, this study demonstrates that the TPR domain of TONSL

406   displays enhanced binding to H3.1K27M compared to WT H3.1. Therefore, it is possible that

407   H3.1K27M directly recruits TONSL to chromatin and form stable complexes that are not inhibited by

408   the post-replicative chromatin maturation step mediated by SET8 via H4K20me1. This hypothesis will

409   need to be tested in cell culture systems, but if confirmed, would support a model where H3.1K27M

410   directly induces misregulation of TONSL activity, which may lead to DNA damage and genomic

411 instability as in plants. Interestingly, our results suggest that the K27M mutation also increase the

412 affinity of TONSL for the H3.3 variant compared to the non-mutated H3.3 protein. Therefore, there is

413 a possibility that H3.3K27M expression may also lead to the misregulation of TONSL, with

414 consequences for genome maintenance.

415

416 Finally, our findings are in line with other studies that point to diverse effects of H3K27M on the

417 regulation of DNA repair pathways and genomic stability (*29-33*). These studies and our work suggest

418 that H3.1K27M not only disrupts cellular identity via loss of H3K27me3, but also modulate the

419 activity of DNA repair pathways to alter genomic integrity and induce tumorigenesis. Although this

420 model underscores the incredible potency of H3K27M in disrupting key biological functions (i.e.,

421 epigenetic programming and genomic stability) required for cellular homeostasis, it also points to new

422 therapeutic routes associated with the DNA damage response that could be applied to help manage or

423 cure cancers characterized by this oncomutation.

424

425

426 **Methods**

427 **Plant materials**

428 Plants were grown at 22 °C under cool-white fluorescent lights (~ 100 µmol m^{-2} s^{-1}) in long-day

429 conditions (16 h light/8 h dark). The T-DNA insertion mutants *atxr5/6* (At5g09790 /At5g24330,

430 SALK_130607/SAIL_240_H01) (*25*), *tsk/bru1-4* (At3g18730, SALK_034207) (*56*), *rad51*

431 (At5g20850, GK_134A01) (*49*), *ku80-7* (At1g48050, SALK_112921) (*57*), *rad17-2* (At5g66130,

432 SALK_009384) (*58*) and *mre11* (At5g54260, SALK_028450) (*59*) are in the Col-0 ecotype

433 background and were obtained from the Arabidopsis Biological Resource Center (Columbus, Ohio).

434 Transgenic plants expressing H3.1 WT (HTR9), H3.1K27M (HTR9 K27M), and H3.1$_{prom}$::H3.3K27M

435 (HTR5 K27M driven by the HTR9 promoter) were made by transforming Col-0 plants or DNA repair

436 mutants (*tsk*, *rad17*, *rad51*, *ku80* and *mre11*).

437

438 **Cloning**

439 To generate transgenic expression constructs (H3.1 WT, H3.1K27M and H3.1$_{prom}$::H3.3K27M), the

440 coding sequences of HTR9 (*At5g10400*) and its promoter (1027 bp upstream of the start codon) were

441 cloned into MoClo system level 0 plasmids pICH41308 and pICH41295, respectively. The H3.1K27M

442 mutation was engineered by site-directed mutagenesis (QuikChange II XL, Agilent Technologies,

443 Santa Clara, CA). The terminator of HSP18.2 (At5g59720, 248 bp downstream of stop codon) was

444 cloned into pICH41276. The level 1 clones were seamlessly assembled using Type-II restriction

445 enzyme BsaI in the order of Promoter-CDS-terminator into destination vector pICH47802. The level

446 1 clones were later assembled into level 2 final clones combined with level 1 Ole::RFP selection

447 cassette using BpiI, which allows for Agrobacterium transformation and RFP selection of

448 transformants in planta.

449

450 To generate TSK/TONSL-TPR and TONSL-TPR+ARD expression constructs, the coding sequences

451 of the TPR domains of *A. thaliana* TSK (aa 1-525) and of mouse TONSL (aa 1-465), and the joint

452 domains TPR+ARD of TONSL (aa 1-693) were cloned into the pET32a vector as previously described

453 (*18*). As for the GST-fused peptides, the coding sequences of the N-terminal tails of *A. thaliana* H3.1

454 (aa 1-58) and H3.3 (aa 1-58) were fused with a C-terminal GST tag by cloning into pET28 as

455 previously described (*18*). The H3.1K27M and H3.3K27M mutations were introduced by site-directed

456 mutagenesis using the QuikChange II XL kit (Agilent Technologies). Briefly, mutagenic primers

22

457   containing the K27M substitution were designed and used for PCR amplification of the plasmid

458   template. The PCR product was then treated with DpnI to digest the parental DNA template, followed

459   by transformation into *E. coli* XL10-Gold ultracompetent cells (Agilent Technologies). The plasmids

460   were sequenced to verify the introduction of the desired mutations.

461

462   For the histone methyltransferase assays, ATXR6 (residues 25-349) was cloned into pGEX-6P as

463   previously described (*25*).

464

465   **Plant transformation**

466   Plant transformations were done using the floral dip method (*60*). Briefly, 400 ml of Agrobacterium

467   (strain GV310) liquid culture grown overnight at 28°C was spun down at 3,220 x g for 25 min and

468   resuspended in 500 mL of transformation solution (5% sucrose and 0.02% Silwet L-77). Arabidopsis

469   flowers were dipped into the bacterial solution for 30 seconds. T1 transgenic plants were selected with

470   the seed specific RFP reporter (OLE1-RFP) with a SFA Light Base (Nightsea, Lexington, MA).

471   Transformations into mutants were either done with homozygous plants (*rad17* and *ku80*) or

472   heterozygous plants (*tsk*, *rad51* and *mre11*), due to low seed set or sterility (*49, 61, 62*). Transgenic

473   *tsk*, *rad51* and *mre11* homozygous plants were identified in the T1 population.

474

475   **Survival assay**

476   Seeds were germinated and grown on ½ MS plates at 22 °C under cool-white fluorescent lights (~ 100

477    $\mu mol\ m^{-2}\ s^{-1}$) in long-day conditions (16 h light/8 h dark) for 5 days, transferred to soil and continued

478   growing under the same conditions. The number of surviving plants were counted on day 0, 4, 8, 12,

479   16, and 20 after transferring to the soil. The survival rate was calculated as the number of live plants

480   divided by the number of total seeds for each genotype.

481

482   **Anthocyanin measurements**

483   Anthocyanin content was determined using a modified version of a previously published protocol (*63*).

484   200 μL of extraction buffer (50% methanol and 5% acetic acid) was added to 50 mg of ground leaf

485   tissue, followed by centrifugation. The supernatant was carefully decanted into a new tube. This step

486   was repeated to ensure complete transfer of the supernatant. Absorbances were measured at 530 nm

487   and 637 nm wavelengths. Anthocyanin concentration, expressed as Abs530 per gram fresh weight (g

488   F.W.), was calculated using the formula [Abs530 - (0.25 × Abs657)] × 5.

489

490   **Comet Assay**

491   DNA damage was assessed in three-week-old plants using a Comet Assay Kit (Trevigen). In brief,

492   leaves were sectioned into small fragments with a razor blade in 500 μl of PBS buffer containing 20

493   mM EDTA and maintained on ice. The nuclei were then released into suspension, filtered through a

494   50 μm nylon mesh into a fresh tube, and subsequently mixed with an equal volume of low-melting-

495   point agarose. The mixture was immediately spread onto CometSlides. Following a 1-hour lysis step

496   at 4°C, the slides were immersed in 1× Tris-acetate electrophoresis buffer for 30 minutes to allow

497   unwinding of the DNA before electrophoresis at 4°C for 10 minutes. Post-electrophoresis, the slides

498   were stained with SYBR Gold for visualization of the nuclei. Imaging was conducted using a Nikon

499   Eclipse Ni-E microscope with excitation at 488 nm. Quantitative analysis of DNA damage was

500   performed using the OpenComet plugin for ImageJ (*64*).

501

MMS genotoxic assay

Seeds were germinated and grown on vertically-oriented ½ MS plates with or without 100μg/ml methyl methanesulfonate (MMS) (Thermo Fisher Scientific, Bohemia, NY) under cool-white fluorescent lights (~ 100 μmol m^{-2} s^{-1}) in long-day conditions (16 h light/8 h dark). Root length measurements were done 10 days (No MMS) or 20 days (100μg/ml MMS) after germination, respectively. The relative root length was calculated by dividing the root length of individual seedlings grown in the presence of MMS by the average root length of plants of the same genotype grown on ½ MS plates.

Somatic recombination assay

H3.1 WT and H3.1K27M transgenic plants were generated by transforming a previously described inverted repeat GUS reporter line (*37*). Experiments were performed at least three times in four-week-old F3 plants as previously described (*18*).

RNA-seq

For each biological replicate, leaves from three plants cultivated in the same flat were combined for RNA extraction using the RNeasy Plant Mini Kit (Qiagen, Hilden, Germany). The integrity of RNA was confirmed with the Agilent 2100 Bioanalyzer Nano RNA Assay (Agilent, Santa Clara, CA). Sequencing libraries were prepared at the Yale Center for Genome Analysis (YCGA) with 200 ng of total RNA using oligo-dT beads for poly A selection. Sequencing (101bp paired-end) was performed on an Illumina NovaSeq X Plus flow cell. Fastp (version 0.21.0 with default parameters) was used to filter and trim paired-end reads (*65*) and reads with quality inferior to 20 were removed. STAR (version 2.7.2a) was used to align the data against the Arabidopsis TAIR10 (*66*) genome with a

25

525   maximum of two mismatches (--outFilterMismatchNmax 2) (*67*). Biological replicates were analyzed

526   for consistency by principal componenet analysis (PCA) using FactoMineR (*68*) The PCA was

527   performed using all genes with an average TPM over ≥ 5 in all samples (fig. S6). For the analysis of

528   the percentage of H3.1 gene transcripts (HTR1, HTR2, HTR3, HTR9, HTR13 and H3.1 transgene),

529   the trimmed reads were mapped and quantified using Salmon (salmon v1.4.0, default parameters) (*69*).

530   For the expression analysis of DNA repair response genes, we utilized a curated list of genes

531   previously assembled by the Britt laboratory. This comprehensive list, accessible via the Britt lab's

532   website (http://brittlab.ucdavis.edu/plant-dna-repair-genes), includes key genes involved in plant

533   DNA repair mechanisms (see Table S1 for the complete gene list). Paired-end fragments

534   corresponding to TEs were determined with featureCounts (version 1.6.4) (*70*). Transposable elements

535   (TEs) were defined as previously described (*71*). TEs were considered to be upregulated if they

536   showed a ≥ 2- fold up-regulation as compared to Col in both biological replicates, and had a value of

537   TPM ≥ 1. The heatmap was generated with the R heatmap.2 function from the ggplot2 package (*72*).

538

539   **Nuclei DAPI staining and Immunostaining**

540   Two-week-old leaves were fixed in 3.7% formaldehyde in cold Tris buffer (10 mM Tris-HCl pH 7.5,

541   10 mM NaEDTA, 100 mM NaCl) for 20 minutes under vacuum. The formaldehyde solution was

542   removed, and leaves were washed twice for 10 minutes in Tris buffer. The leaves were chopped using

543   razor blades in 150 μl LB01 buffer (15 mM Tris-HCl pH7.5, 2 mM NaEDTA, 0.5 mM spermine-

544   4HCl, 80 mM KCl, 20 mM NaCl and 0.1% Triton X-100), then filtered through a 30 μm mesh (Sysmex

545   Partec, Gorlitz, Germany). 10 μl of lysate was added to 10 μl of sorting buffer (100 mM Tris-HCl pH

546   7.5, 50 mM KCl, 2mM $MgCl_2$, 0.05% Tween-20 and 5% sucrose) and dried onto a coverslip for 30

547   minutes. Cold methanol was added onto each coverslip for 3 minutes. Methanol was aspirated and

548 TBS-Tx (20 mM Tris pH 7.5, 100 mM NaCl, 0.1% Triton X-100) was added for 5 minutes. TBS-Tx

549 was then removed. For DAPI staining only, the coverslips were immediately mounted onto slides with

550 Vectashield mounting medium with DAPI (Vector Laboratories, Burlingame, CA). For

551 immunostaining experiments, the following steps were performed: the coverslips were blocked by

552 adding 75 µl of Abdil-Tx (2% BSA in TBS-Tx) to each coverslip for 30 minutes, followed by a 1 hour

553 incubation with the appropriate primary antibody (H3K27me1; Active Motif #61015, H3K27me3,

554 Millipore #07-449, H3K27M, Active Motif #61803) diluted in Abdil-Tx. The coverslips were then be

555 washed with TBS-Tx. 30 µl of secondary antibody was added on each coverslip and incubated for 30

556 minutes followed by washing with TBS-Tx. Finally, the coverslips were mounted onto slides with

557 Vectashield mounting medium with DAPI. Images (Z-series optical sections of 0.3 µm steps) were

558 taken on a Nikon Eclipse Ni-E microscope with a 100X CFI PlanApo Lamda objective (Nikon, Minato

559 City, Tokyo, Japan) equipped an Andor Clara camera. Images were deconvolved using the imageJ

560 deconvolution plugin.

561

562 **ChIP-seq**

563 ChIP was performed as described previously (*73*), with some modifications. Briefly, rosette leaves

564 from 2-week-old plants were fixed for 15 min in 1% formaldehyde, followed by flash freezing.

565 Approximately 0.1 g of ground tissue was added to 10 mL of extraction buffer 1 (0.4 M sucrose, 10

566 mM Tris–HCl, 10 mM $MgCl_2$) and filtered through a 40 μm mesh. Samples were centrifuge at

567 3,000g for 20 min. The pellets were resuspended in 1 mL of extraction buffer 2 (0.25 M sucrose, 10

568 mM Tris–HCl, 10 mM $MgCl_2$, 1% Triton X-100) and centrifuged at 12,000g for 10 min. 400 μL of

569 extraction buffer 3 (1.7 M sucrose, 10 mM Tris-HCl (pH8.0), 0.15% Triton X-100) was used to

570 resuspend the pellets. The homogenate was added to a fresh tube containing 400 μL of extraction

27

571   buffer 3, followed by centrifugation for 1 h at 16,000g. The pellets were resuspended in nuclei lysis

572   buffer (50 mM Tris–HCl pH 8.0, 10 mM EDTA, 1% SDS), and chromatin was sheared using a

573   Bioruptor 200 sonicator (20 times on a 30-s ON, 30-s OFF cycle). The supernatants were centrifuged

574   at 16,000g for 5 min. ChIP dilution buffer (1.1% Triton X-100, 1.2 mM EDTA, 16.7 mM Tris–HCl

575   pH 8.0, 167 mM NaCl) was added to the supernatant to obtain 10× volume. Antibodies (2 μL of

576   H3K27me3 antibody (Millipore #07-449) or 2 μL of H3K27me1 antibody (ABclonal A22170) were

577   added to 750 μL of diluted sample and incubated at 4°C overnight. An equal amount of drosophila

578   chromatin (Active Motif #53083) was added to each sample to allow for quantitative comparisons of

579   samples displaying very different amounts of H3K27 methylation marks (ChIP-Rx) (*74*).

580   Immunoprecipitation was performed using protein A magnetic beads (New England BioLabs, Ipswich,

581   MA). The beads were washed, resuspended in 200 μL of elution buffer (1% SDS and 0.1-M NaHCO$_3$)

582   and incubated at 65°C for 15 min for elution. After uncrosslinking, samples were treated with

583   proteinase K and purified using a ChIP DNA Clean and Concentrator kit (Zymo Research, Irvine,

584   CA).

585

586   ChIP sequencing libraries were prepared at the YCGA with a TruSeq Library Prep Kit (Illumina, San

587   Diego, CA). They were validated using an Agilent Bioanalyzer 2100 High sensitivity DNA assay, and

588   quantified using the KAPA Library Quantification Kit for Illumina® Platforms kit. Sequencing was

589   done on an Illumina NovaSeq 6000 using the S4 XP workflow. Fastp (version 0.21.0 with default

590   parameters) was used to filter and trim paired-end reads (*65*). The reads with quality scores < 20 were

591   removed. Duplicate reads were also removed using the Picard toolkit

592   (https//broadinstitute.github.io/picard) (MarkDuplicates with REMOVE_DUPLICATES=true). To

593   calculate the Rx scaling factor of each biological replicate, Drosophila-derived IP read counts were

594   normalized to the number of input reads. Spike-in normalization was performed as previously

595   described (*75, 76*). We used $\alpha = r/Nd\_IP$ (*74*) to compute the scaling factor α for each replicate, with

596   Nd_IP corresponding to the number of reads (in millions) aligning to the *D. melanogaster* genome in

597   the IP and with $r = 100 * Nd\_i / (Na\_i + Nd\_i)$, where Nd_i and Na_i are the number of input reads

598   (in millions) aligning to the *D. melanogaster* or *A. thaliana* genome, respectively. We generated

599   bedgraph files with a bin size of 10 bp using deepTools (*77*) using Rx factors to scale each of the

600   samples. The plot profile and heatmap in Fig. 2B were generated using deeptools. In order to generate

601   the chromosomal representation in Figure 2C, featureCounts (version 1.6.4) was used to count the

602   paired-end reads within 100-kb regions of the genome and scaled by adjusting the number of reads in

603   each bin with Rx factors Consistency between biological replicates was confirmed by Pearson

604   correlation using deepTools2 (fig. S7) (*77*).

605

Histone protein extraction

607   Histone protein extraction was performed as previously described (*78*) with some modifications. For

608   each sample, approximately 80 mg of plant material was ground with 1 ml of cold Nuclear Isolation

609   Buffer (NIB) (*78*) and transferred to a 2-ml Dounce homogenizer. The plant homogenate was then

610   processed with a loose pestle in the Dounce homogenizer for 50 strokes on ice. The lysate was filtered

611   through two layers of Miracloth into new tubes and centrifuged. The supernatant was discarded, and

612   the pellet was washed three times with NIB. The nuclear pellet was then resuspended in 1 ml of 0.4 N

613   H_2SO_4. This mixture was transferred to a 2-ml Dounce homogenizer and homogenized with 40

614   strokes on ice to disrupt the nuclei. After centrifugation, the supernatant was transferred to a fresh tube

615   and mixed with 264 μl of trichloroacetic acid dropwise to precipitate the proteins. The mixture was

616   incubated on ice for 3 hours to ensure complete precipitation. Following incubation, the histone pellet

617   was centrifuged at 14,000 rpm for 15 minutes at 4°C. The supernatant was carefully removed, and the

618   pellet was washed with 500 μl of ice-cold acetone to remove any remaining acid and impurities. The

619   acetone wash step was repeated once more to ensure thorough cleaning. The pellet was then air-dried

620   at room temperature until no visible moisture remained. Finally, the dried histone pellet was

621   resuspended in 25 μl of histone storage buffer (10 mM Tris-HCl, pH 7.5, 0.1 mM EDTA) for storage

622   at -80°C.

623

624   **Western blotting**

625   Total histone samples were subjected to Western blot analysis. Laemmli sample buffer (Bio-Rad,

626   Hercules, CA) was added to each total histone sample, incubated at 95°C for 3 minutes, and loaded

627   onto a 4%-20% gradient SDS-PAGE gel. Following electrophoresis, proteins were transferred onto

628   membranes using a semi-dry blotter in Tris-glycine transfer buffer containing 20% methanol. The

629   membranes were then blocked with 5% non-fat dry milk in TBST (20 mM Tris-HCl, pH 7.6, 150 mM

630   NaCl, 0.1% Tween-20) for 1 hour at room temperature to prevent non-specific binding. The

631   membranes were then probed with H3K27me1(Active Motif: 61015) or H3K27me3 (Millipore: 07-

632   449) for 1 hour, followed by incubation with a secondary HRP-labeled antibody (Sigma) at a 1:10 000

633   dilution for 1 hour at room temperature. Blots were visualized using the Bio-Rad Clarity Western ECL

634   Substrate and imaged with a Bio-Rad ChemiDoc MP Imaging System. Relative quantification of

635   Western blot bands was performed with Image J.

636

637   **Nucleosome assembly**

638   Recombinant nucleosome arrays for histone methyltransferase assays were assembled as described

639   previously (*79*). In short, histones were expressed in *E. coli* and purified from inclusion bodies.

640   Histone octamers consisting of Arabidopsis H2A.13 (At3g20670), H2B (At3g45980), and Xenopus

641   H4 along with either Xenopus H3 fused to a C-terminal Strep tag (H3-CT Strep) or Arabidopsis H3.1

642   (At1g09200) with K27A or K27M mutations were reconstituted by dialysis into refolding buffer (10

643   mM Tris pH 8, 1 mM EDTA, 5 mM b-mercaptoethanol, 2 M NaCl) and purified by size exclusion

644   chromatography on a Superdex 200 gel filtration column (GE Healthcare). To form nucleosome

645   arrays, histone octamers were assembled onto a plasmid containing 12 repeats of the 601 nucleosome

646   positioning sequence connected via a 30-bp linker using gradient dialysis from 2 M to 0.4 M NaCl

647   followed by a step dialysis into TE.

648

649   **Histone methyltransferase assay**

650   Histone methyltransferase assays were performed as previously described (*80*). Briefly, 0.5 ug of

651   GST-ATXR6 and 0.5 ug of H3-CT-Strep nucleosomes were added to a total reaction volume of 25 ul.

652   We either added no inhibitor, or 0.5 ug of K27A or K27M nucleosomes. The reactions were incubated

653   for 1 h at 30 °C. SDS-PAGE sample buffer was added to each tube followed by heating to 95°C for 5

654   min. Samples were resolved by SDS-PAGE (15% gels) and transfered to a PVDF membrane.

655   Coomassie stain solution (45% methanol, 10% acetic acid, 0.25% Coomassie Brilliant Blue R) was

656   used to stain the membrane followed by destaining (45% methanol, 10% acetic acid). Membranes

657   were air-dried, sprayed with EN³HANCE (Perkin Elmer) and exposed to autoradiography film

658   overnight at -80 °C. Films were developed and bands were quantified using the software ImageJ.

659

660   **Flow cytometry**

661   Rosette leaves from two-week-old plants were finely chopped in 0.2 – 0.5 ml Galbraith buffer (45 mM

662   MgCl2, 20 mM MOPS, 30 mM sodium citrate, 0.1% Triton X-100, 40 µg/ml RNase A) and filtered

663   through a 30 μm mesh (Sysmex Partec). Isolated nuclei were stained by adding 20 μg/ml propidium

664   iodide (Sigma) to each sample, followed by vortexing. The samples were analyzed using BD

665   FACSAria II sorter (Becton Dickinson, Franklin Lakes, NJ). FlowJo 10.9.0 (Tree Star, Ashland,

666   Oregon) was used to generate profiles and for quantification (nuclei counts and rCV values). Each

667   biological replicate represents one plant.

668

669   **DNA-seq**

670   Genomic DNA was extracted as previously described (*81*). For each biological replicate, 5 plants were

671   pooled to obtain approximately 40 mg of leaf tissue. DNA sequencing libraries were prepared at the

672   YCGA. Genomic DNA was sonicated to an average fragment size of 350 bp using a Covaris E220

673   instrument (Covaris, Woburn, MA). The libraries were generated using the xGen Prism library prep

674   kit for NGS (Integrated DNA Technologies, Coralville, IA). Paired-end 150 bp sequencing was

675   performed on an Illumina NovaSeq 6000 using the S4 XP workflow (Illumina, San Diego, CA). Raw

676   FASTQ data were filtered and trimmed using the fastp tool (--length_required 20, --

677   qualified_quality_phred 20) (*65*). The filtered sequences were then mapped to the genome (TAIR10)

678   using BWA-MEM default parameters (https://doi.org/10.48550/arXiv.1303.3997). Mapped reads

679   were sorted, duplicates were removed and indexed using SAMtools (*82*). Biological replicates were

680   analyzed for consistency with deepTools2 (fig. S8) (*77*). The program featurecount (version 2.0.6)

681   (*70*) was used to count the paired-end fragments present in each 50-kb region of the *A. thaliana*

682   genome as previously described (*18*). The log2 ratio was centered on the average ratio of any two

683   compared libraries normalized to the first 5 Mbp of chromosome 1. Plot profiles were generated using

684   R (version 4.3.2) (*83*) and Gviz (*84*).

685

32

686   **Protein expression**

687   Plant histones-GST fusion proteins and AtTSK-TPR were expressed in Rosetta (DE3) E. coli (Sigma,

688   St. Louis, MO). The bacterial cultures were grown in Luria-Bertani (LB) medium, and expression of

689   the fusion proteins were induced with 1 mM isopropyl β-D-1-thiogalactopyranoside (IPTG) at room

690   temperature. Human histones-GST fusion proteins, mouse TONSL-TPR, mouse TONSL-TPR+ARD

691   were expressed in ArcticExpress (DE3) E. coli (Agilent, Santa Clara, CA). The expression of human

692   histones-GST fusion proteins, TONSL-TPR and TONSL-TPR+ARD were expressed at 16 °C for 24

693   hours and induced with IPTG (1mM) at OD_{600nm}= 0.4.

694

695   To purify the histone-GST fusion proteins, harvested cell pellets were resuspended in PBS (1X

696   Phosphate-Buffered Saline: 137 mM NaCl, 10 mM phosphate, 2.7 mM KCl, pH 7.4) supplemented

697   with 1 mM phenylmethylsulfonyl fluoride (PMSF) prior to lysis by sonication and clarification by

698   centrifugation. The clear lysate was then applied to a Glutathione Sepharose 4B affinity column. After

699   thorough washing with PBS to remove unbound material, the fusion proteins were eluted with Elution

700   Buffer (EB: 50 mM Tris-HCl, 50 mM NaCl, 30 mM reduced L-Glutathione, 10% glycerol, pH 8.0).

701   The eluted proteins were then concentrated using Amicon® Ultra Centrifugal Filter Units

702   (MilliporeSigma) with a 10 kDa molecular weight cutoff. The elution buffer was replaced with storage

703   buffer (50 mM Tris-HCl, 50 mM NaCl, 10% glycerol, pH 8.0) by centrifuging at 4,000 x g for 20

704   minutes. The concentrated and purified proteins were aliquoted and preserved at -80°C for long-term

705   storage.

706

707   ATXR6 expression in *E.coli* and purification was described in detail in a previous publication (*25*).

708   The purification of AtTSK-TPR, TONSL-TPR and TONSL-TPR+ARD (containing an N-terminal

33

709   Trx-His-S tag and a C-terminal His tag) was performed as previously described with minor

710   modifications (*18*). Briefly, the cell pellets were resuspended in NPI-10 buffer (50 mM NaH$_2$PO$_4$, 300

711   mM NaCl, 10 mM imidazole, pH 8.0) containing 1 mM PMSF, and sonicated for 2.5 min (30 s pulse,

712   1 min break, 5 cycles). After centrifugation, the supernatant was transferred into a new 50 ml Falcon

713   tube and added with washed agarose Ni-NTA His beads. The expressed proteins were trapped after

714   passing through the Ni-NTA agarose column. The column was then washed by 7.5 ml NPI-20 (50 mM

715   NaH2PO4, 300 mM NaCl, 20 mM imidazole, pH 8.0) twice, and eluted with 10 ml NPI-250 buffer

716   (50 mM NaH2PO4, 300 mM NaCl, 250 mM imidazole, pH 8.0). The eluted proteins were further

717   concentrated using Amicon Ultra Centrifugal Filter (50 kDa) to 1.5 ml for size exclusion

718   chromatography (SEC). The concentrated proteins were injected onto SEC and eluted using a SEC

719   buffer (25mM Hepes, 200mM NaCl, pH 7.5). Peak fractions from the S200 column were pooled,

720   concentrated to 1-2 mg ml^{-1}, flash frozen under liquid nitrogen and stored at −80 °C.

721

722   **Histone binding assays**

723   For the TSK$_{TPR}$ -histone binding assays, 2 μg of AtTSK were combined with either 2 μg of GST or

724   GST-tagged histone tails (aa 1 to 58 of plant H3.1) in 400 μl of binding buffer (25 mM Tris-HCl, 250

725   mM NaCl, 0.05% NP-40, pH 8.0). The mixture was incubated overnight at 4°C with rotation.

726   Subsequently, 15 μl of pre-washed Glutathione Sepharose 4B agarose beads (Cytiva, Marlborough,

727   MA) were added to each sample and incubated for 30 minutes to pull-down the GST-tagged proteins.

728   The beads were then washed four times for 5 minutes with 1 mL of binding buffer, while rotating at

729   4°C. The final wash was performed with binding buffer containing 150 mM NaCl. The proteins were

730   eluted with 15 μl of 2× SDS loading buffer and denatured by boiling at 95°C for 5 minutes. Samples

731   were then resolved on a 10% SDS-PAGE gel. The lower section of the gel underwent Coomassie

34

732 staining to assess the GST and GST-tagged proteins, while the upper section was analyzed by Western

733 blot using an anti-His antibody (Sigma; H1029). The TONSL$_{TPR +ARD}$ and TONSL$_{TPR}$ binding assays

734 were performed as described above with the following modifications. The binding buffer consisted of

735 50 mM Tris-HCl pH8.0, 300 mM NaCl, 5% glycerol, 0.25% NP-40, 0.2 mM EDTA, 1 mM DTT. The

736 binding reaction was incubated for 2 hours at 4°C. The samples were resolved on a 4-20% gradient

737 gel. Each pull-down experiment was repeated a minimum of three times.

738

739 **Nucleosome binding assay**

740 The nucleosome binding assays were performed as described for the histone binding assays with

741 TONSL$_{TPR +ARD}$. The Recombinant human biotinylated nucleosomes were obtained from EpiCypher

742 (Durham, NC).

743

744 **Split-luciferase complementation assays**

745 The TPR domain (aa 1-524) of TSK, fused with a nuclear localization signal (NLS), and the NLS

746 alone, were cloned into the Gateway destination vector pGWB-cLUC (Addgene Plasmid #174051).

747 Histones H3.1 and H3.1K27M (aa 1-136) were inserted into the Gateway destination vector pGWB-

748 nLUC (Addgene Plasmid #174050). Agrobacterium tumefaciens GV3101 strains harboring these

749 constructs were introduced into the leaves of 4-week-old Nicotiana benthamiana plants. For co-

750 infiltration experiments, Agrobacterium cultures adjusted to cell densities of 0.1–0.5 at OD600 were

751 mixed in equal volumes. To inhibit gene silencing, the tomato bushy stunt virus (TBSV) p19 silencing

752 suppressor, encoded within the pDGB3alpha2_35S:P19:Tnos vector (Addgene Plasmid #68214), was

753 also included in the infiltration mixture. The Agrobacterium inoculum was prepared by resuspension

754 in infiltration buffer (10 mM MgCl2, 10 mM MES, pH 5.6, and 150 μM acetosyringone) and incubated

35

755 at room temperature for 2 hours. The inoculum was then gently infiltrated into the abaxial side of the

756 leaves using a 1 ml needleless syringe. At 48-72 hours post-infiltration, a 1 mM luciferin solution was

757 applied to the leaves. Before imaging, detached leaves were kept in darkness for 10 minutes to reduce

758 chlorophyll fluorescence interference. Luminescence was captured with a charge-coupled device

759 (CCD) camera. Image analysis and quantification were performed using ImageJ software.

760

761 **RT-qPCR**

762 RNA was isolated from two-week-old leaf tissue using TRIzol (Invitrogen, Carlsbad, CA). RNA

763 samples were treated with RQ1 RNase-free DNase (Promega, Madison, WI) at 37°C for 30 min. 750

764 ng of total RNA was used to produce cDNA with iScript cDNA Synthesis Kit (Bio-Rad, Hercules,

765 CA). Real-time PCR was done using KAPA SYBR FAST qPCR Master Mix (2X) Kit (Kapa

766 Biosystems, Wilmington, MA) on a CFX96 Real-Time PCR Detection System (Bio-Rad, Hercules,

767 CA). Relative quantities were calculated using the Ct method with *ACTIN7* (*At5g09810*) as the

768 normalizer (*85*). At least three biological replicates were performed for each experiment.

Primer name	Sequence
ACTIN-F	TCGTGGTGGTGAGTTTGTTAC
ACTIN-R	CAGCATCATCACAAGCATCC
H3.1-Transgene-F	ACACAAACTTAAGCACACAACCT
H3.1-Transgene-R	TGCCTAAGGATATCCAGCTTGCGAGG

769

770

771 **Plant genotyping**

772 Leaves from 2 or 3-week-old plants were homogenized in 500 μl DNA extraction buffer (200 mM

773 Tris-HCl (pH 8.0), 250 mM NaCl, 25 mM EDTA and 1% SDS) and 50 μl phenol:chloroform:isoamyl

774 alcohol (25:24:1). Each sample was centrifuged for 10 min at 15,000 rpm. 350 μl of the aqueous layer

775 was transferred to a 1.5 ml tube containing 350 μl isopropanol. Samples were then mixed, incubated

776   at room temperature for 15 min and then spun down at 15,000 rpm for 10 min. The supernatant was

777   removed to secure the pellets. 400 μl 70% ethanol was used to wash the pellets. After centrifugation

778   at 15,000 rpm for 5 min, the ethanol was removed and the pellets were dissolved in 50 μl water.

779   Genotypes of individual T-DNA insertion T1 transgenic plants were determined by running two sets

780   of genotyping PCR using GoTaq DNA polymerase (Promega, Madison, WI). WT primer sets amplify

781   the original sequence of the given genes, while the mutant primer sets amplify the mutated sequence

782   with T-DNA insert.

Primer name	Sequence
TSK-WT-F	TAACTGCTTGTTGGTTGTCCC
TSK-WT-R	ACGACGACCAGTTGTTTCAAC
tsk-M-F	TGGTTCACGTAGTGGGCCATCG
tsk-M-R	ACGACGACCAGTTGTTTCAAC
MRE11-WT-F	CCAGAAGAACTGAACCAGCAG
MRE11-WT-R	CACTTTTGAAGGCAGCTGAAG
mre11-M-F	TGGTTCACGTAGTGGGCCATCG
mre11-M-R	CACTTTTGAAGGCAGCTGAAG
RAD51-WT-F	CGAGGAAGGATCTCTTGCAG
RAD51-WT-R	GAGAGCAAACCTGTGCCAAT
rad51-M-F	CGAGGAAGGATCTCTTGCAG
rad51-M-R	ATATTGACCATCATACTCATTGC

783

784

Data availability

786   Sequencing data (RNA-seq, ChIP-seq and DNA-seq datasets) generated for this study are available

787   from the SRA under accession numbers PRJN1121202. Additional materials reported in this study are

788   available upon request from the corresponding author.

789

790

791

792

793

37

References

1. D. N. Louis *et al.*, cIMPACT-NOW update 2: diagnostic clarifications for diffuse midline glioma, H3 K27M-mutant and diffuse astrocytoma/anaplastic astrocytoma, IDH-mutant. *Acta Neuropathol* **135**, 639-642 (2018).

2. J. Schwartzentruber *et al.*, Driver mutations in histone H3.3 and chromatin remodelling genes in paediatric glioblastoma. *Nature* **482**, 226-231 (2012).

3. G. Wu *et al.*, Somatic histone H3 alterations in pediatric diffuse intrinsic pontine gliomas and non-brainstem glioblastomas. *Nat Genet* **44**, 251-253 (2012).

4. D. Castel *et al.*, Histone H3F3A and HIST1H3B K27M mutations define two subgroups of diffuse intrinsic pontine gliomas with different prognosis and phenotypes. *Acta Neuropathol* **130**, 815-827 (2015).

5. S. Bender *et al.*, Reduced H3K27me3 and DNA hypomethylation are major drivers of gene expression in K27M mutant pediatric high-grade gliomas. *Cancer Cell* **24**, 660-672 (2013).

6. K. M. Chan *et al.*, The histone H3.3K27M mutation in pediatric glioma reprograms H3K27 methylation and gene expression. *Genes Dev* **27**, 985-990 (2013).

7. P. W. Lewis *et al.*, Inhibition of PRC2 activity by a gain-of-function H3 mutation found in pediatric glioblastoma. *Science* **340**, 857-861 (2013).

8. S. Venneti *et al.*, Evaluation of histone 3 lysine 27 trimethylation (H3K27me3) and enhancer of Zest 2 (EZH2) in pediatric glial and glioneuronal tumors shows decreased H3K27me3 in H3F3A K27M mutant glioblastomas. *Brain Pathol* **23**, 558-564 (2013).

9. A. Ebert *et al.*, Su(var) genes regulate the balance between euchromatin and heterochromatin in Drosophila. *Genes Dev* **18**, 2973-2983 (2004).

10. K. J. Ferrari *et al.*, Polycomb-dependent H3K27me1 and H3K27me2 regulate active transcription and enhancer fidelity. *Mol Cell* **53**, 49-62 (2014).

11. X. Shen *et al.*, EZH1 mediates methylation on histone H3 lysine 27 and complements EZH2 in maintaining stem cell identity and executing pluripotency. *Mol Cell* **32**, 491-502 (2008).

12. D. Pasini *et al.*, Characterization of an antagonistic switch between histone H3 lysine 27 methylation and acetylation in the transcriptional regulation of Polycomb group target genes. *Nucleic Acids Res* **38**, 4958-4969 (2010).

13. F. Tie *et al.*, CBP-mediated acetylation of histone H3 lysine 27 antagonizes Drosophila Polycomb silencing. *Development* **136**, 3131-3141 (2009).

14. A. S. Harutyunyan *et al.*, H3K27M in Gliomas Causes a One-Step Decrease in H3K27 Methylation and Reduced Spreading within the Constraints of H3K36 Methylation. *Cell Rep* **33**, 108390 (2020).

15. A. S. Harutyunyan *et al.*, H3K27M induces defective chromatin spread of PRC2-mediated repressive H3K27me2/me3 and is essential for glioma tumorigenesis. *Nat Commun* **10**, 1262 (2019).

16. A. Loyola, G. Almouzni, Marking histone H3 variants: how, when and why? *Trends Biochem Sci* **32**, 425-433 (2007).

17. A. Loyola, T. Bonaldi, D. Roche, A. Imhof, G. Almouzni, PTMs on H3 variants before chromatin assembly potentiate their final epigenetic state. *Mol Cell* **24**, 309-316 (2006).

836   18.   H. Davarinejad *et al.*, The histone H3.1 variant regulates TONSOKU-mediated DNA repair
837   during replication. *Science* **375**, 1281-1286 (2022).
838   19.   E. Duro *et al.*, Identification of the MMS22L-TONSL complex that promotes homologous
839   recombination. *Mol Cell* **40**, 632-644 (2010).
840   20.   B. C. O'Connell *et al.*, A genome-wide camptothecin sensitivity screen identifies a
841   mammalian MMS22L-NFKBIL2 complex required for genomic stability. *Mol Cell* **40**, 645-657
842   (2010).
843   21.   L. O'Donnell *et al.*, The MMS22L-TONSL complex mediates recovery from replication stress
844   and homologous recombination. *Mol Cell* **40**, 619-631 (2010).
845   22.   W. Piwko *et al.*, RNAi-based screening identifies the Mms22L-Nfkbil2 complex as a novel
846   regulator of DNA replication in human cells. *Embo J* **29**, 4210-4222 (2010).
847   23.   G. Saredi *et al.*, H4K20me0 marks post-replicative chromatin and recruits the TONSL-
848   MMS22L DNA repair complex. *Nature* **534**, 714-718 (2016).
849   24.   Y. Jacob *et al.*, Selective methylation of histone H3 variant H3.1 regulates heterochromatin
850   replication. *Science* **343**, 1249-1253 (2014).
851   25.   Y. Jacob *et al.*, ATXR5 and ATXR6 are H3K27 monomethyltransferases required for
852   chromatin structure and gene silencing. *Nat Struct Mol Biol* **16**, 763-768 (2009).
853   26.   Y. Jacob *et al.*, Regulation of heterochromatic DNA replication by histone H3 lysine 27
854   methyltransferases. *Nature* **466**, 987-991 (2010).
855   27.   H. Stroud *et al.*, DNA methyltransferases are required to induce heterochromatic re-
856   replication in Arabidopsis. *PLoS Genet* **8**, e1002808 (2012).
857   28.   D. Hanahan, R. A. Weinberg, Hallmarks of cancer: the next generation. *Cell* **144**, 646-674
858   (2011).
859   29.   I. Bockaj *et al.*, The H3.3K27M oncohistone affects replication stress outcome and provokes
860   genomic instability in pediatric glioma. *PLoS Genet* **17**, e1009868 (2021).
861   30.   G. Giacomini *et al.*, Aberrant DNA repair reveals a vulnerability in histone H3.3-mutant brain
862   tumors. *Nucleic Acids Res*, (2024).
863   31.   S. N. Grobner *et al.*, The landscape of genomic alterations across childhood cancers. *Nature*
864   **555**, 321-327 (2018).
865   32.   A. Mackay *et al.*, Integrated Molecular Meta-Analysis of 1,000 Pediatric High-Grade and
866   Diffuse Intrinsic Pontine Glioma. *Cancer Cell* **32**, 520-537 e525 (2017).
867   33.   Y. Zhang *et al.*, Histone H3K27 methylation modulates the dynamics of FANCD2 on
868   chromatin to facilitate NHEJ and genome stability. *J Cell Sci* **131**, (2018).
869   34.   D. Sanders *et al.*, Histone Lysine-to-Methionine Mutations Reduce Histone Methylation and
870   Cause Developmental Pleiotropy. *Plant Physiol* **173**, 2243-2252 (2017).
871   35.   T. Okada, M. Endo, M. B. Singh, P. L. Bhalla, Analysis of the histone H3 gene family in
872   Arabidopsis and identification of the male-gamete-specific variant AtMGH3. *Plant J* **44**, 557-
873   568 (2005).
874   36.   Z. Li, G. J. Ahammed, Plant stress response and adaptation via anthocyanins: A review. *Plant
875   Stress* **10**, 100230 (2023).
876   37.   J. M. Lucht *et al.*, Pathogen stress increases somatic recombination frequency in
877   Arabidopsis. *Nat Genet* **30**, 311-314 (2002).
878   38.   Y. Jacob, S. D. Michaels, H3K27me1 is E(z) in animals, but not in plants. *Epigenetics* **4**, 366-
879   369 (2009).

39. V. Sahu, C. Lu, Oncohistones: Hijacking the histone code. *Annu Rev Cancer Biol* **6**, 293-312 (2022).

40. P. Fransz, J. H. De Jong, M. Lysak, M. R. Castiglione, I. Schubert, Interphase chromosomes in Arabidopsis are organized as well defined chromocenters from which euchromatin loops emanate. *Proc Natl Acad Sci U S A* **99**, 14584-14589 (2002).

41. M. Ingouff *et al.*, Zygotic resetting of the HISTONE 3 variant repertoire participates in epigenetic reprogramming in Arabidopsis. *Curr Biol* **20**, 2137-2143 (2010).

42. A. M. Lindroth *et al.*, Dual histone H3 methylation marks at lysines 9 and 27 required for interaction with CHROMOMETHYLASE3. *Embo J* **23**, 4286-4296 (2004).

43. Z. Z. Brown *et al.*, Strategy for "detoxification" of a cancer-derived histone mutant based on mapping its interaction with the methyltransferase PRC2. *J Am Chem Soc* **136**, 13498-13501 (2014).

44. N. Justin *et al.*, Structural basis of oncogenic histone H3K27M inhibition of human polycomb repressive complex 2. *Nat Commun* **7**, 11316 (2016).

45. J. M. Stafford *et al.*, Multiple modes of PRC2 inhibition elicit global chromatin alterations in H3K27M pediatric glioma. *Sci Adv* **4**, eaau5935 (2018).

46. W. Feng *et al.*, Large-scale heterochromatin remodeling linked to overreplication-associated DNA damage. *Proc Natl Acad Sci U S A* **114**, 406-411 (2017).

47. M. E. Potok *et al.*, The role of ATXR6 expression in modulating genome stability and transposable element repression in Arabidopsis. *Proc Natl Acad Sci U S A* **119**, (2022).

48. C. Raynaud *et al.*, Two cell-cycle regulated SET-domain proteins interact with proliferating cell nuclear antigen (PCNA) in Arabidopsis. *Plant J* **47**, 395-407 (2006).

49. W. Li *et al.*, The Arabidopsis AtRAD51 gene is dispensable for vegetative development but required for meiosis. *Proc Natl Acad Sci U S A* **101**, 10596-10601 (2004).

50. M. van Kregten *et al.*, T-DNA integration in plants results from polymerase-theta-mediated DNA repair. *Nat Plants* **2**, 16164 (2016).

51. M. E. Luedeman *et al.*, Poly(ADP) ribose polymerase promotes DNA polymerase theta-mediated end joining by activation of end resection. *Nat Commun* **13**, 4547 (2022).

52. L. S. Symington, J. Gautier, Double-strand break end resection and repair pathway choice. *Annu Rev Genet* **45**, 247-271 (2011).

53. A. Syed, J. A. Tainer, The MRE11-RAD50-NBS1 Complex Conducts the Orchestration of Damage Signaling and Outcomes to Stress in DNA Replication and Repair. *Annu Rev Biochem* **87**, 263-294 (2018).

54. P. Bundock, P. Hooykaas, Severe developmental defects, hypersensitivity to DNA-damaging agents, and lengthened telomeres in Arabidopsis MRE11 mutants. *Plant Cell* **14**, 2451-2462 (2002).

55. Y. C. Huang, W. Yuan, Y. Jacob, The Role of the TSK/TONSL-H3.1 Pathway in Maintaining Genome Stability in Multicellular Eukaryotes. *Int J Mol Sci* **23**, (2022).

56. K. Brzezinka, S. Altmann, I. Baurle, BRUSHY1/TONSOKU/MGOUN3 is required for heat stress memory. *Plant Cell Environ* **42**, 771-781 (2019).

57. S. Valuchova *et al.*, Protection of Arabidopsis Blunt-Ended Telomeres Is Mediated by a Physical Association with the Ku Heterodimer. *Plant Cell* **29**, 1533-1545 (2017).

58. F. Heitzeberg *et al.*, The Rad17 homologue of Arabidopsis is involved in the regulation of DNA damage repair and homologous recombination. *Plant J* **38**, 954-968 (2004).

924   59.   I. Samanic, J. Simunic, K. Riha, J. Puizina, Evidence for distinct functions of MRE11 in
925   Arabidopsis meiosis. *PLoS One* **8**, e78760 (2013).
926   60.   S. J. Clough, A. F. Bent, Floral dip: a simplified method for Agrobacterium-mediated
927   transformation of Arabidopsis thaliana. *Plant J* **16**, 735-743 (1998).
928   61.   S. Takeda *et al.*, BRU1, a novel link between responses to DNA damage and epigenetic gene
929   silencing in Arabidopsis. *Genes Dev* **18**, 782-793 (2004).
930   62.   J. Puizina, J. Siroky, P. Mokros, D. Schweizer, K. Riha, Mre11 deficiency in Arabidopsis is
931   associated with chromosomal instability in somatic cells and Spo11-dependent genome
932   fragmentation during meiosis. *Plant Cell* **16**, 1968-1978 (2004).
933   63.   M. Nakata, M. Ohme-Takagi, Quantification of Anthocyanin Content. *Bio-protocol* **4**, e1098
934   (2014).
935   64.   B. M. Gyori, G. Venkatachalam, P. S. Thiagarajan, D. Hsu, M. V. Clement, OpenComet: an
936   automated tool for comet assay image analysis. *Redox Biol* **2**, 457-465 (2014).
937   65.   S. Chen, Y. Zhou, Y. Chen, J. Gu, fastp: an ultra-fast all-in-one FASTQ preprocessor.
938   *Bioinformatics* **34**, i884-i890 (2018).
939   66.   P. Lamesch *et al.*, The Arabidopsis Information Resource (TAIR): improved gene annotation
940   and new tools. *Nucleic Acids Res* **40**, D1202-1210 (2012).
941   67.   A. Dobin *et al.*, STAR: ultrafast universal RNA-seq aligner. *Bioinformatics* **29**, 15-21 (2013).
942   68.   S. Lê, J. Josse, F. Husson, FactoMineR: An R Package for Multivariate Analysis. *Journal of
943   Statistical Software* **25**, 1–18 (2008).
944   69.   M. Noda *et al.*, Salmon: scalable ab-initio light-matter simulator for optics and nanoscience.
945   *Computer Physics Communications* **235**, 356-365 (2019).
946   70.   Y. Liao, G. K. Smyth, W. Shi, featureCounts: an efficient general purpose program for
947   assigning sequence reads to genomic features. *Bioinformatics* **30**, 923-930 (2014).
948   71.   K. Panda *et al.*, Full-length autonomous transposable elements are preferentially targeted
949   by expression-dependent forms of RNA-directed DNA methylation. *Genome Biol* **17**, 170
950   (2016).
951   72.   H. Wickham, *ggplot2*. (Springer New York, New York, 2009), pp. VIII, 213.
952   73.   C. B. Villar, C. Kohler, Plant chromatin immunoprecipitation. *Methods Mol Biol* **655**, 401-411
953   (2010).
954   74.   D. A. Orlando *et al.*, Quantitative ChIP-Seq normalization reveals global modulation of the
955   epigenome. *Cell Rep* **9**, 1163-1170 (2014).
956   75.   J. Dong *et al.*, H3.1K27me1 maintains transcriptional silencing and genome stability by
957   preventing GCN5-mediated histone acetylation. *Plant Cell* **33**, 961-979 (2021).
958   76.   A. Nassrallah *et al.*, DET1-mediated degradation of a SAGA-like deubiquitination module
959   controls H2Bub homeostasis. *Elife* **7**, (2018).
960   77.   F. Ramirez *et al.*, deepTools2: a next generation web server for deep-sequencing data
961   analysis. *Nucleic Acids Res* **44**, W160-165 (2016).
962   78.   R. Scheid *et al.*, Histone Acid Extraction and High Throughput Mass Spectrometry to Profile
963   Histone Modifications in Arabidopsis thaliana. *Curr Protoc* **2**, e527 (2022).
964   79.   P. Voigt *et al.*, Asymmetrically modified nucleosomes. *Cell* **151**, 181-193 (2012).
965   80.   Y. Jacob, P. Voigt, In Vitro Assays to Measure Histone Methyltransferase Activity Using
966   Different Chromatin Substrates. *Methods Mol Biol* **1675**, 345-360 (2018).

81. J. D. Clarke, Cetyltrimethyl ammonium bromide (CTAB) DNA miniprep for plant DNA isolation. *Cold Spring Harb Protoc* **2009**, pdb prot5177 (2009).

82. H. Li *et al.*, The Sequence Alignment/Map format and SAMtools. *Bioinformatics* **25**, 2078-2079 (2009).

83. R. C. Team, R: A language and environment for statistical computing. R Foundation for Statistical Computing, Vienna, Austria., (2018).

84. F. Hahne, R. Ivanek, Visualizing Genomic Data Using Gviz and Bioconductor. *Methods Mol Biol* **1418**, 335-351 (2016).

85. K. J. Livak, T. D. Schmittgen, Analysis of relative gene expression data using real-time quantitative PCR and the 2(-Delta Delta C(T)) Method. *Methods* **25**, 402-408 (2001).

Acknowledgments

Author contributions

Y.J. supervised the work, and conceptualized the study and the experiments with Y.C.H. and W.Y. All the experiments were performed by W.Y., Y.C.H., and C.L. The genomic analyses were done by A.P. and W.Y. The nucleosomes arrays were generated by D.V. and P.V. Funding for the project was

993   secured by Y.J., J.v.W., and P.V. The manuscript was written by Y.J. and C.L, with contributions from

994   W.Y. and Y.C.H.

995

Ethics declarations

997   The authors declare no competing interests.

998

Supplementary information

1000   Figs. S1 to S8

1001   Tables S1 to S2

1002